The Pennsylvania State University

The Graduate School

Department of Engineering Science and Mechanics

FABRICATION AND CHARACTERIZATION OF HIGH DAMPING CARBON FIBER COMPOSITES WITH CARBON NANOTUBE INTERLAYERS

A Thesis in

Engineering Science and Mechanics

by

Jeffrey J. Kim

Submitted in Partial Fulfillment

of the Requirements

for the Degree of

Master of Science

May 2019

The thesis of Jeffrey J. Kim was reviewed and approved* by the following:

Charles E. Bakis
Distinguished Professor of Engineering Science and Mechanics
Thesis Co-Advisor

Edward C. Smith
Professor of Aerospace Engineering
Thesis Co-Advisor

Namiko Yamamoto
Assistant Professor of Aerospace Engineering

Judith A. Todd
P.B. Breneman Chair and Professor of Engineering Science and Mechanics
Head of the Department of Engineering Science and Mechanics

*Signatures are on file in the Graduate School

ABSTRACT

Carbon/epoxy (c/ep) composite rotorcraft blades, consisting of carbon fibers in a matrix of epoxy, are commonly used to manufacture rotorcraft blades because of their good balance of mass, stiffness, and strength properties. Recent interest in rigid (hingeless) rotorcraft blades has brought attention to the need for higher amounts of damping in c/ep rotorcraft blades. Previous investigations have demonstrated that adding small amounts of carbon nanotubes (CNTs) to epoxy increases damping without degrading stiffness by a combined effect of reinforcement and stick-slip behavior at the CNT/epoxy interface. Limited evidence in the literature suggests that CNTs increase the damping of c/ep composites, as well, although a more thorough investigation aimed maximizing the improvement in c/ep damping with CNTs and assessing damping behavior over a range of simulated operating conditions for rotorcraft blades is required to advance the state-of-the-art.

The objectives of this investigation are to explore in detail the potential of CNTs for increasing the damping of c/ep laminates across a range of loading and environmental conditions. Because of the strain sensitivity of the stick-slip damping mechanism of CNTs and the high force required to develop meaningful strains in c/ep laminates, tensile tests in a servo-hydraulic load frame were used to acquire cyclic force and strain data as functions of time. Software was written to extract the phase shift between force and load along with the storage modulus (E'), loss modulus (E''), and loss factor ($\tan \delta$) under particular loading regimens and environmental conditions. Three types of CNTs, long CNT buckypaper, short CNT buckypaper, and aligned CNT yarn, and two types of surfactants, Triton X-100 and sodium dodecyl sulfate, were the primary material variations investigated. The combination of CNT yarn and Triton X-100 was selected over the other material variations due to its superior damping performance. The addition

of 10 vol.% of aligned CNT yarn in $[0/\pm45]_s$ c/ep laminates increased tan δ and (E'') as much as 310% and 340%, respectively with negligible change in E' and tensile strength. Following 10^6 cycles of strain excursions between 300 με and 4000 με in the $[0/\pm45]_s$ laminate with YN10%-TX4, tan δ increased by 42% versus the initial tan δ. Similear YN10%-TX4 laminates showed moderate increases in tan δ and E'' as temperature was increased to 65°C.

TABLE OF CONTENTS

LIST OF FIGURES

LIST OF TABLES

ACKNOWLEDGEMENTS

This research is supported by the Government under Agreement No. W911W6-17-2-0003. The U.S. Government is authorized to reproduce and distribute reprints notwithstanding any copyright notation thereon. The views and conclusions contained in this document are those of the author and should not be interpreted as representing the official policies, either expressed or implied, of the U.S. Government.

I would like to thank first and foremost my advisors Dr. Charles E. Bakis and Dr. Edward C. Smith, for providing the opportunity to perform this research and also giving me advice on my research through weekly VLRCOE meeting. Both of my advisors have been examples of a true researcher and have encouraged me with endless amount of patience. I also thank Dr. Namiko Yamamoto for serving on the committee.

I thank Dr. Anirrudh Vashisth for mentoring me until his graduation in the Fall of 2017. I thank Keerti Prakash for the discussions on the theory of CNT damping. I also thank Jinhoo Kim and Ian Mckinney for their help in the lab. I would like to acknowledge Rudy Haluza for always actively engaging with the lab members in the lab.

I would like to thank my parents Getchoon Kang and Shinwoo Kim, and my sister Jamie Kim for always encouraging me. I am grateful for having lived in State College, which has been a place full of good people. State College has given me so many memories I can and will never forget.

Last but not least, I thank Jesus Christ, the Savior of my life, for never letting me go even in the times I've wanted to give up and run away. Even though I cannot see him, touch him, or hear him, God was gracious enough to give me faith and let me realize that I am not just a random speck of dust in the universe made without any purpose but rather a precious creation longing to get back to the Creator.

Chapter 1

Introduction

1.1 Background

1.1.1 Vibration of Structures

Carbon/epoxy (c/ep) composite, compared to traditional metals, is a well-known material for lightweight structures due to its high strength to weight ratio (Daniel et al. 1994). Moreover, the fatigue resistance of c/ep adds another value to structures that experience prolonged exposure to vibration (Foye and Shipley 1981). As a result, rotorcraft blades generating tremendous amount of vibration are often manufactured with c/ep composites. Among various types of rotorcraft, co-axial configuration with rigid hingeless blades, which by design has two rotors on top of each other, is an important area of research because it can allow high speed forward flight (Paglino 1971, Kim et al. 2009). Although the co-axial configuration could be also made with hinged articulated blades, this type of blades is not desirable due to excessive flapping, unlike rigid hingeless blades, which have inherent aerodynamic damping for the flap modes (Blackwell and Millott 2008). For this reason, the distance between the two sets of blades can be close enough to prevent aerodynamic drags without increasing collision risks. Nonetheless, this design still faces a critical roadblock – when the rigid hingeless blades are configured, they do not provide sufficient edgewise damping in the first lag mode (Abbe et al. 1977). The vibrations due to lack of damping in the lead-lag direction can not only lead to short fatigue life of blades at the root but also cause instabilities such as ground and air resonance. Therefore, improving the damping behavior of rigid rotorcraft blades has attracted much attention in the rotorcraft industry.

In recent decades, several approaches have been implemented to minimize the vibration. For example, hydraulic and viscoelastic passive dampers offer advantages and disadvantages of their own. Hydraulic dampers are able to add sufficient amount of damping and yet require complex design, weight penalty, and regular maintenance for wear and tear of seals (McGuire 1994). Viscoelastic dampers, on the other hand, are lightweight and have simple configuration but produce relatively low damping, which is also sensitive to temperature (Almeras 1997, Kulak and Hughes 1993). Both of the approaches are inadequate for rigid hingeless configuration because the small range of motion due to the high bending stiffness of the blades limits the damping effect. In recent advancement, active control dampers made of piezoelectric ceramic are being noticed as an optimistic candidate for the lead-lag damper as they can minimize vibrations by generating counteractive isotropic strains on the surface of blades (Chopra 2002). However, such ceramic materials still possess drawbacks – the short fatigue life from the inherent brittleness of the materials and the need for a complex configuration due to their dependence on power supply. As a result, a better method of adding damping to the system without leading to weight penalty, complex design, or temperature sensitivity is much needed and appreciated for designing the next generation of high-performance rotorcrafts.

1.1.2 Definition of dynamic properties

It is important to address and define dynamic properties since the measure of damping behavior can be described in multiple ways. The complex modulus approach is one of the methods damping of materials is measured (Jones 2001, Menard 2008). When oscillatory force is applied to a material under the assumption of linear viscoelasticity, there exist two extreme situations. The first situation is the complete elastic case in which the energy from the applied

force is fully stored in the material and therefore induce in-phase sine waves of the applied stress and the strain as shown in Figure 1-1a.

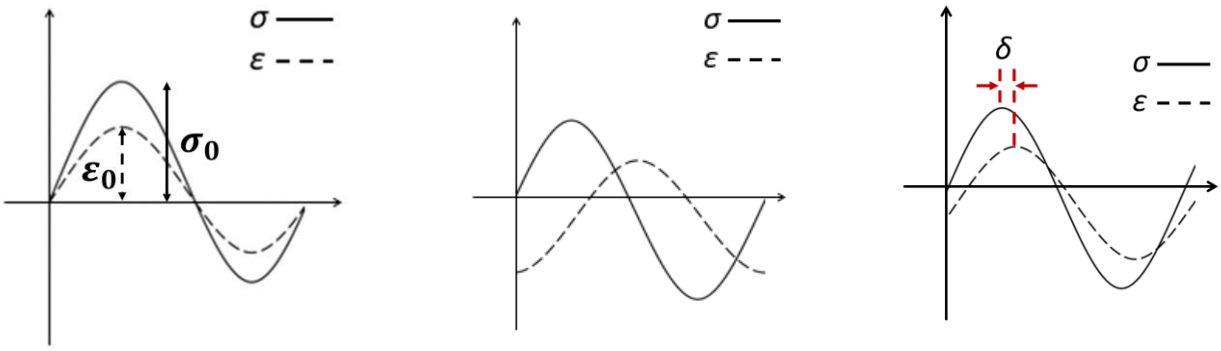

(a) Elastic behavior where $\delta = 0°$ (b) Viscous behavior where $\delta = 90°$ (c) Viscoelastic behavior

Figure 1-1: Representation of dynamic properties.

The second situation is the completely viscous case where the material dissipates the energy from the oscillation, resulting in 90° out-of-phase sine waves of the stress and strain (Figure 1-1b). However, most materials particularly polymers contain both elastic and viscous behavior, which is the intermediate of two extreme cases (Figure 1-1c). As a result, such viscoelastic materials partially recover the energy and dissipate rest of the energy from the system. The recovered and dissipated energy are represented by storage modulus (E') and loss modulus (E''), respectively, making up the complex modulus (E^*) (Equation 1~3).

$$E^* = E' + iE'' \quad (1)$$

$$E' = E^* \cos\delta \quad (2)$$

$$E'' = E^* \sin\delta \quad (3)$$

Furthermore, the ratio of E' and E'' is called loss factor (tan δ) where the phase difference (δ) between the two curves indicates the degree of damping. The wider the difference is, the higher

the damping becomes. Like any other complex number, these moduli in addition to the phase difference can be visually described with the trigonometry (Figure 1-2). However, due to the anisotropic behavior of c/ep laminate, loss factor can vary with respect to directions. As an example, Table 1-1 shows the loss factor in the longitudinal, transverse, and shear directions of the unidirectional c/ep laminate that was tested at room temperature with free-free flexural mode either in bending or torsion (Ni and Adams 1984). As can be seen, the typical trend is that the loss factor in the longitudinal or the fiber direction is the lowest among three because the high stiffness and low loss factor of fibers dominate the overall damping behavior of the laminate. Meanwhile, the shear damping has the highest loss factor of all.

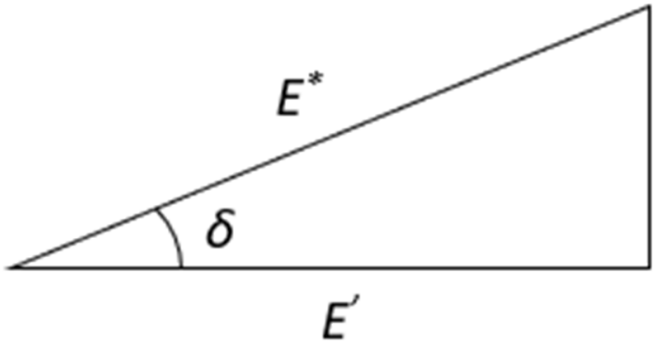

$$E^* = \frac{\sigma_0}{\varepsilon_0}$$

Figure 1-2: Diagram representing the trigonometric relationship of the complex modulus.

Table 1-1: Loss factor in the longitudinal, transverse, and shear direction from Ni and Adams (1984).

Material	tan $\delta^{\dagger}$ longitudinal	transverse	shear
c/ep composite (HMS/DX-210)	0.00072	0.00672	0.0112

[†]The original data were given in specific damping capacity (ψ), which was converted to tan δ by using the unit conversion, tan $\delta = \psi/(2\pi)$

1.1.3 CNT Damping – Stick Slip Mechanism

Through recent modeling and experimental work, carbon nanotubes (CNTs) have been recognized as lightweight passive damping materials for polymeric materials due to their high strength, high stiffness, and low density. CNTs are divided into two categories: single-walled carbon nanotubes (SWCNT) and multi-walled carbon nanotubes (MWCNT). SWCNT has only one wall with a typical diameter of 1 nm whereas MWCNT has multiple layers of walls with a typical diameter of 10 nm (Mousa 2018). Stiffness of 1 TPa and tensile strength as high as 100 GPa make CNTs a promising candidate for dissipating energy and adding damping through interfacial interactions (Lu 1997, Yu et al. 2000, Koratkar et al 2002, Zhou et al. 2004, Wang et al. 2010). The process of dissipating energy can be divided into a couple of steps. At the initial stage when a low load is applied to the system, CNTs and the matrix elongate together without having a damping contribution. As more load is applied to the material, there comes a point where the load overcomes the critical shear stress, which is the amount of shear stress required for the CNTs to slip relative to the matrix. At this point, the load does not transfer to the CNTs anymore but the matrix material continues to stretch. This slippage phenomenon causes friction motion between the two materials, consequently dissipating energy. When the unloading occurs, the CNTs stick to the matrix through the van der Waals bond, and the same process begins again in the opposite direction. In situations where sinusoidal vibration is applied to the system, the reversible phenomenon, also known as the stick-slip mechanism, will continue to add damping. The type and the strength of bond between the CNTs and the matrix are the two sources that determine the success of the stick-slip mechanism. Having the covalent bond induces only a one-time event, whereas the weak van der Waals bond induces reversible process in which CNTs could stick back to the matrix as the material gets constantly loaded and unloaded. The van der Waals force, which is a weak electrostatic force that forms between materials close to each other,

between the CNT and the matrix is necessary in order to maintain the reversible process of the stick-slip mechanism. Since the development of the stick-slip model of CNT-matrix interactions, the physical behavior of CNTs damping was further incorporated in models that considered alignment of CNTs, aspect ratio, the CNT volume content, and the adjustment of critical shear stress (Liu et al. 2006, Liu et al. 2010, Ogasawara et al. 2011, Alva and Raja 2014, Glaz et al. 2015, Gardea et al. 2015, Prakash et al. 2018, Prakash et al 2019).

Along with the improvement of stick-slip models, the experimental work simultaneously showed significant increase in damping from CNTs. Since the initial report of damping increase of CNT films (Koratkar et al. 2002), the additional damping from CNTs have gradually advanced and become more relevant to structural applications. For example, Suhr et al. 2005 reported 1400% damping tan δ increase with 50 vol.% of CNT in polymethylacrylate and ethyl-2-cyanoacrylate (PMA-ECA). Rajoria and Jalili 2005 also reported 700% increase in the damping ratio using the log decrement method from adding 7.5 wt.% of CNT in amine cured epoxy resin, using the dispersion technique. However, the addition of continuous fibers reduced the influence of CNTs on the overall behavior of composite materials dominated by the fiber stiffness (Khan et al. 2011).

To the best of author's knowledge, Devalve and Pitchumani 2013 was the first group who demonstrated a significant improvement of 133% increase in tan δ by dispersing 2 wt.% CNT in the cross-ply carbon/epoxy composite, although not as impressive as the improvement shown in only the matrix materials without continuous fibers. In addition to the dominant presence of fibers, low CNT loading is believed to be the major source that limits the damping increase. However, the CNT dispersion technique often increases the viscosity level of matrix to the point where wetting continuous fibers becomes infeasible. For this reason, feasible methods of incorporating CNTs into c/ep composites were explored in order to add significant amount of CNTs for damping. Some of the interesting forms of CNTs were buckypaper and yarn. It should

be noted that these previous studies were conducted with test methods such the log decrement and the dynamic mechanical analysis in bending that cause bending strain which is nonuniform throughout the gage section and therefore not appropriate for nonlinear damping like stick-slip damping. Applying uniform strain throughout the gage section was an important factor in this investigation.

1.1.4 Fabrication of CNT Buckypaper and Yarn

As the resin viscosity dramatically increases due to the significantly high surface area of CNTs, alternative techniques for increasing the CNT loading in c/ep composites are needed to maximize the benefit of increasing damping behavior through stick-slip mechanism. Even though Rajoria and Jalili 2005 managed to add 7.5 wt.% of CNTs in epoxy resin through dispersion technique, the CNT loading was reduced even further down to only a couple of weight percentage once continuous fibers are introduced (Khan et al. 2011, Devalve and Pitchumani 2013). One of the alternative methods discovered was the fabrication of CNTs in the form of a sheet known as buckypaper (Wang et al. 2004). The highly concentrated CNT buckypaper is often fabricated through vacuum filtration and can be placed between fiber prepregs from which excess epoxy resin impregnates buckypaper, increasing the overall CNT loading of a c/ep composite. Although easily torn at low force, buckypaper nevertheless has enough structural integrity that prevents CNT washout caused by the flow of the resin during various manufacturing procedures. In one study, nearly 39 wt.% of CNT was added in epoxy resin (Wang et al. 2004). Moreover, another study more relevant to c/ep composite has increased CNT loading to as high as 8 wt.% in a c/ep laminate with 45 wt.% carbon fibers (Wang et al. 2015). The novel method of fabricating CNTs in buckypaper enabled much higher CNT concentration than the dispersion technique.

Although not as popular as the buckypaper, CNTs were fabricated in a yarn form. The CNT yarns are made through procedures such as wet-spinning, spinning from a CNT-grown mat, and spinning from CNT aerogels (Zhang et al. 2004). In one study, CNT yarns were wound to fabricate a CNT yarn/epoxy composite, completely replacing continuous carbon fibers (Kim et al. 2016). This achievement opened the opportunity in combining CNT yarns and carbon fibers for damping behavior, as the damping of CNT yarns have yet to be investigated, to the best of the author's knowledge.

1. 2 Objectives

The objective of the research is to investigate the stick-slip effect of high CNT concentration on the damping behavior of c/ep composites by experimentally evaluating different types of material under various testing conditions. The following tasks are needed to tackle the current investigation:

1. Develop a servo-hydraulic tension test setup for characterizing the dynamic behavior of c/ep composites and perform damping tests in tension-tension mode to maintain uniform strain field through the gage section.
2. Develop a high quality specimen fabricating method for complete control of overall constituents and verify good resin impregnation with low void content.
3. Evaluate the dynamic properties of c/ep laminate with high CNT concentration through methods such as buckypaper and yarn interlayers.
4. Investigate the effect of strain variation, temperature, and fatigue on the dynamic properties.

Chapter 2

Specimen Preparation

2.1 Materials

Baseline prepreg of c/ep composite consisted of standard modulus T700SC-12K-50C carbon fiber from Toray (Tacoma, WA) and diglycidyl ether of bisphenol F epoxide (EPON 862) cured with diethyltoluenediamine curing agent (EPIKURE W), both of which were purchased from Hexion (Columbus, OH). The viscosity of the resin mixture with the stochiometric mix ratio of 100:26.4 (resin:curing agent) is 21-23 P at 25°C (Miller-Stephenson, 2012). Dry spun multi-walled carbon nanotube (MWCNT) yarn and MWCNT buckypaper were selected as the type of CNT for the damping augmentation due to their structural integrity that prevents the CNTs from migrating to other locations during the curing process (Figure 2-1). Miralon YM 2-ply yarn from Nanocomp Technologies Inc. (Marrimack, NH) was 150 μm in diameter (Nanocomp Technologies, 2016). 20 gsm Long-MWCNT buckypaper was purchase from NanoTechLabs Inc. (Yadkinville, NC) (NanoTechLabs, 2017). Short MWCNT buckypaper was made in-house through the vacuum filtration process with short MWCNT with the diameter of 20-30 nm purchased from Cheap Tubes Inc. (Grafton, VT). The aspect ratio of the pristine short MWCNT was between 1:17 and 1:100, although the sonication process is expected to shorten the aspect ratio (Sharma 2010). Graphene buckypaper (Conductive Graphene sheets, 8”×4”), purchase from Graphene Supermarket (Calverton, NY), was also used as a source for producing additional damping through stick-slip mechanism.

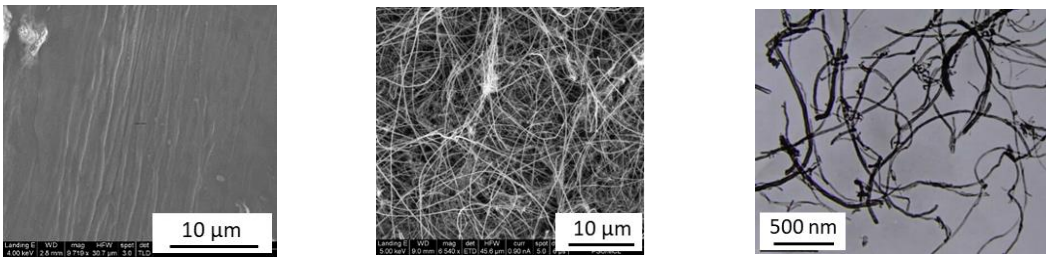

a) b) c)

Figure 2-1: Microscopic image of a) Miralon CNT yarn, b) long CNT buckypaper, and c) short CNT buckypaper. Figure 2-1c) was reprinted with permission from Cheap Tubes (2019). Copyright 2019 Cheap Tubes Inc.

Surfactant was used in order to disperse CNTs and also to modify the interfacial bond strength between the CNTs and the matrix because the addition of surfactant introduces steric hindrance, which provides repulsive forces between the CNTs, and hydrogen bonding between the CNTs and surfactant (Gong et al. 2000, Rastogi et al. 2008, Poutrel et al. 2017). Widely used surfactants, polyoxyethylene octyl phenyl ether, Triton X-100 (TX), with critical micelle concentration (CMC) of 0.2 to 0.9 mM and sodium dodicyl sulfate (SDS) with CMC of 7 to 10 mM were purchased from Sigma-Aldrich (St. Louis, MO). Although the surfactants ultimately mix with epoxy resin, the surfactant concentration was selected based on the information about the CNTs dispersed in acetone and surfactant (Geng et al. 2008). In order to achieve CMC of Triton X-100, 0.125 mg of Triton X-100 in 1 mL of acetone is required. Based on this information, it was found that 4.375 mg of SDS in 1 mL of acetone is required to maintain CMC of SDS, assuming CMC is 7 mM. It was also assumed that the ratio of the mass of the surfactant to the volume of the acetone was the same as the ratio of the mass of the surfactant to the volume of the epoxy. The critical hemimicelle concentration (HMC) is the state in which the surfactants cover the surface area of absorbent, in this case the CNTs (Parfitt and Rochester 1983; Berg 2010). As CMC and HMC are related, the surfactant that leads to CMC faster than the other often times have the same trend with the HMC (Adair 2019). Even though the HMC was not measured, the information about the CNT dispersion in acetone was used to select the surfactant concentration.

In addition, seven damping materials besides the nanomaterials for stick-slip mechanisms were also investigated (Table 2-1). Polyurethane (PU) veil, core-shell rubber (CSR), nano-silica (NS), and viscoelastic damping polymer (VDP) were explored to obtain additional damping through the viscoelastic behavior. Although NS is purely elastic and brittle material, it adds damping in the epoxy resin from the shear strain generated at the filler-matrix interface (Suhr et al. 2006). Binary alloy NiTi shape memory alloy (SMA) wire from Shape Memory Applications (Santa Clara, CA) was explored to exploit additional damping from the movement of the martensite/martensite twin interfaces under low strain, which ultimately dissipated energy through heat (Van Humbeeck 2003). Soft lead zirconate titanate (PZT) powder, donated by TRS Technologies (State College, PA) was also explored because PZT materials were reported to add passive damping to c/ep composites through electrical and thermal dissipation (Tanimoto et al. 1997). The specification of the PZT can be found in Table A-15. As reported by Tanimoto (2007), the addition of PZT C-82 particles from Fuji ceramic in the interlayer of c/ep composites generated current when the composite was vibrated at a resonant frequency. Tanimoto found that the addition of 9 gsm of PZT in each interlayer of $[0°/90°]_s$ laminate led to 300% tan δ increase at the first resonant frequency.

Table 2-1: Seven exploratory damping materials other than CNTs.

Damping material	Vendor	Product	Damping mechanism
SMA wire	Shape Memory Applications	MCF0109	Phase transformation
PZT powder	TRS	Type II 207	Thermal dissipation from electrical resistance
PU veil	BASF	Elastolan 1185 A-10X	Viscoelastic stress relaxation
CSR	Kaneka	MX-135	Viscoelastic stress relaxation
NS	3M	Matrix resin 4833	Viscoelastic stress relaxation
VDP	3M	F9469PC VHB	Viscoelastic stress relaxation
Graphene	Graphene Supermarket	Conductive graphene sheets	Stick-slip

2.2 Short Buckypaper Fabrication

Buckypaper was fabricated in-house with short aspect ratio CNTs because short CNT buckypaper was not commercially available at the time of this investigation. The vacuum filtration process to make the short CNT buckeypapers is illustrated in Figure 2-2.

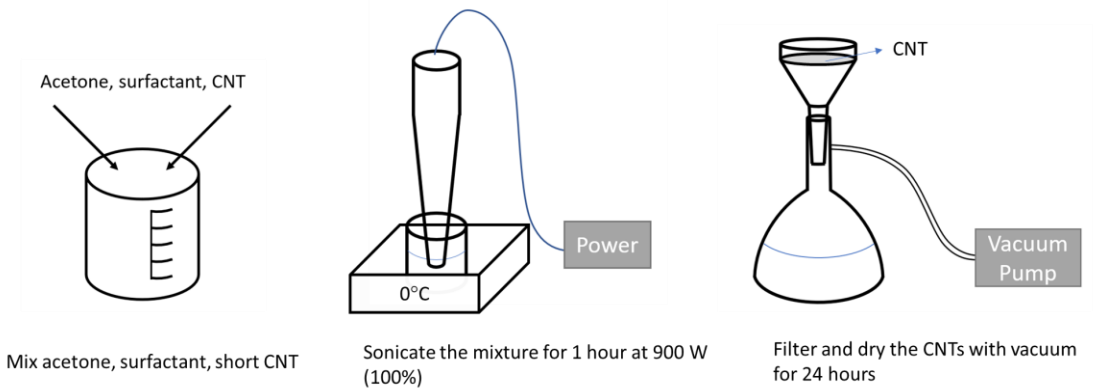

Figure 2-2: Overview of vacuum filtration process for making short CNT buckypapers.

0.265 g of short CNTs in the filter paper with the area of 0.0133 m^2 were mixed in 400 ml acetone with 1:0.76 mass ratio of CNT : surfactant to get 20 grams per square meter (gsm), which matches the areal density of the long CNT buckypaper. Branson 184 V tip sonicator was used to sonicate the mixture in 800 ml beaker that was immersed in an ice water bath (Figure 2-3). The CNT mixture was poured over a pre-weighed Whatman 1006-150 filter paper that, in turn, was placed in a 130 mm diameter Buchner funnel on top of a flask. Vacuum was then pulled on the flask for 15 minutes to draw the mixture through the filter. The buckypaper was then dried for 24 hours with the vacuum running under a fume hood. In order to get the mass of the buckypaper, the filter paper was weighed before and after transferring the CNTs onto the prepreg, and the mass of the CNT was obtained by subtracting the two weighed masses. Then the buckypaper and the filter paper were cut in five 2.54 × 2.54 cm^2 squares. It must be noted, however, that the use

of vacuum process led to formation of “mud-cracks” on the buckypaper. As a result, the filter paper had to be gently flipped onto the prepreg.

Figure 2-3: Branson 184 V 900 W 20 kHz tip sonicator.

2.3 C/ep Prepregs

Carbon fiber prepregs were wound in-house with a McClean Anderson winding machine on a 25.4-cm-diameter by 76.2-cm-long aluminum cylindrical mandrel that was pre-wrapped with a non-porous PTFE cloth (Figure 2-4 and Figure 2-5).

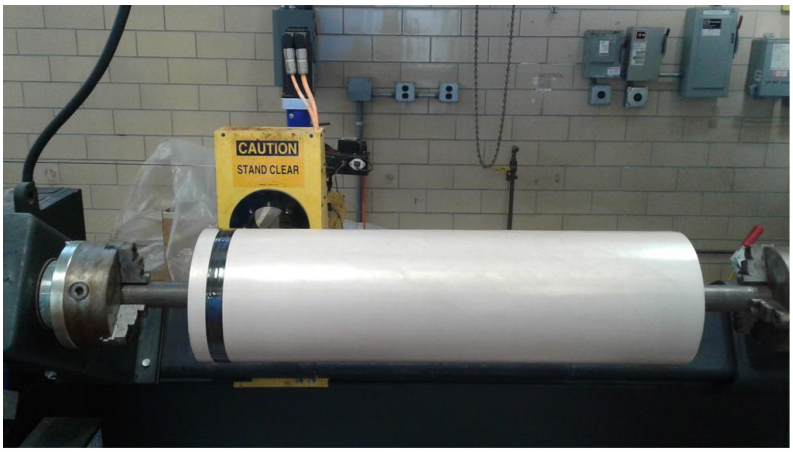

Figure 2-4: Wet filament winding carbon tow onto a round mandrel to make prepreg. McClean Anderson winding machine.

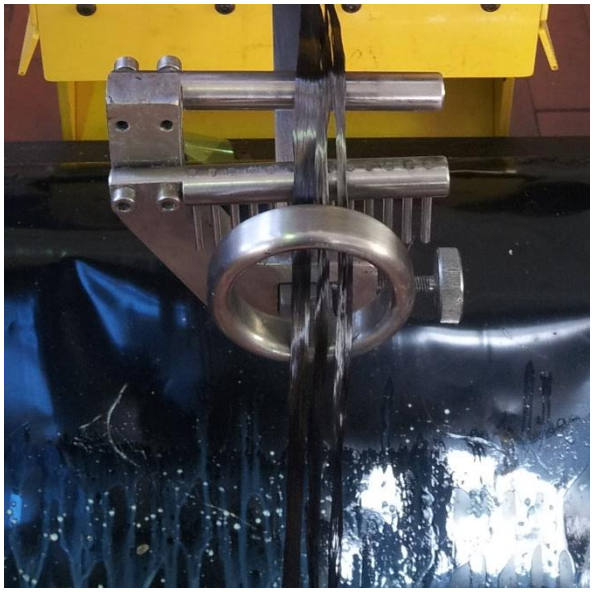

Figure 2-5: Payout eye used during the fabrication process to control the movement of the tow and to impregnate the tow with resin.

862/W Mixture of EPON 862 (862) and EPIKURE W (W) were mixed with the 100:26.4 stoichiometric ratio in 800 ml plastic beaker for 5 minutes using an electric hand drill with a plastic impeller (Figure 2-6). In the case of the specimen with CSR, MX-135 resin containing 25 wt.% CSR and W curative were mixed with the 100:19.6 stoichiometric ratio (MX-135:W). In the

case of the specimen with both CSR and NS, MX-135, 3M 4833 containing 42 wt.% NS, and W curative were mixed with the 62.7:37.3:17.9 stoichiometric ratio (MX-135: 3M 4833:W).

Figure 2-6: Mixing resin with an electric drill.

Resin was poured into a single-tow resin bath. The temperature of the resin bath was kept at room temperature due to the low viscosity of the resin. The temperature should be increased to 66°C for better resin impregnation if the vacuum process is absent after the prepreg is manufactured. As seen in Figure 2-7, 0.2-cm diameter and 0.119-cm-diameter orifices were inserted at the entrance and at the exit, respectively, for a smooth guidance of the tow through the center of the bath as well as for providing a wet fiber volume fraction (V_{f_wet}) of 41.5% as shown in Equation 4,

$$V_{f\_wet} = \frac{A_t}{A_o} \cdot 100\% = \frac{nd_f^2}{d_o^2} \cdot 100\% \quad (4)$$

where

A_t = area of the tow

A_o = area of the orifice

n = number of fibers in a tow = 12000

d_f = diameter of the fiber = 7 μm

d_o = diameter of the exit orifice

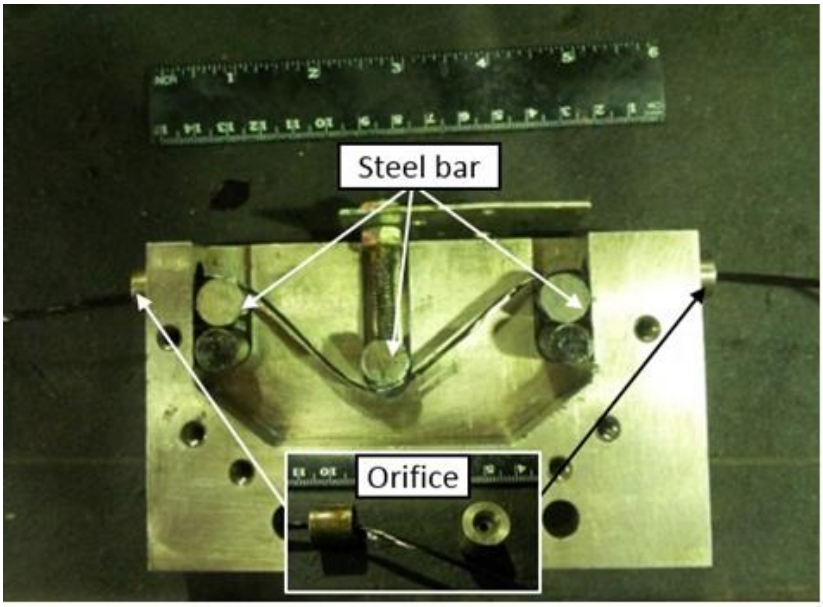

Figure 2-7: Single tow resin bath.

The tow traveled through a payout eye, after which the end of the tow was taped onto the mandrel pre-wrapped with a sheet of non-porous PTFE cloth. The tension force was set at only 4.5 N (1 lbf) in order to prevent the tow from vibrating. However, higher tension force than 4.5 N would be required to get acceptably low void content in the prepreg if the degassing process was not performed at a later stage of laminate fabrication. It should be noted that the maximum load that a tow can take depends on various parameters such as the rotational speed of the mandrel, the type of the tow, the orifice diameter, the viscosity of resin, and the inclusion of fillers. However, from the author's previous experience, applying more than 31 N (7 lbf) tension force on a single

T700SC-12K-50C carbon fiber tow leads to fiber fraying and breakage. Fibers with the programmed bandwidth of 0.229 cm were wound on the mandrel at the rotational speed of 7 rpm, resulting in a single layer unidirectional fiber prepreg of 363 gsm. Once the prepreg was wound, it was vital to turn off the tension force first and foremost before cutting the fibers because otherwise, the wet fiber tow would rapidly coil back to the spool in the tensioner as the resin splashes every single place that the resin rich tow makes contact. With the tension force turned off, the prepreg was cut open along the length of the mandrel, after which a sheet of vacuum bag material was placed over the top of the prepreg (Figure 2-8).

Figure 2-8: Prepreg covered with vacuum bag.

In order to conveniently store the prepreg in a freezer at -19°C, it was cut into 4-inch-wide strips, which were stacked together. The stack was then wrapped with another piece of vacuum bag material and then sealed with tacky tape for later use. Although the prepregs become flexible again in room temperature, the prepregs start to stiffen even in room temperature if they are stored too long. It is recommended that the 862/W system be discarded after being stored in the freezer for 6 months.

2.4 C/ep Composite Laminate

Figure 2-9 describes the procedure for manufacturing c/ep composite laminates of various stacking sequences. The $[0/\pm45]_s$ laminate was selected to be representative of a typical rotorcraft blade layup (Liu and Haftka 2004). The other unidirectional laminates were selected to predict the multi-directional laminate.

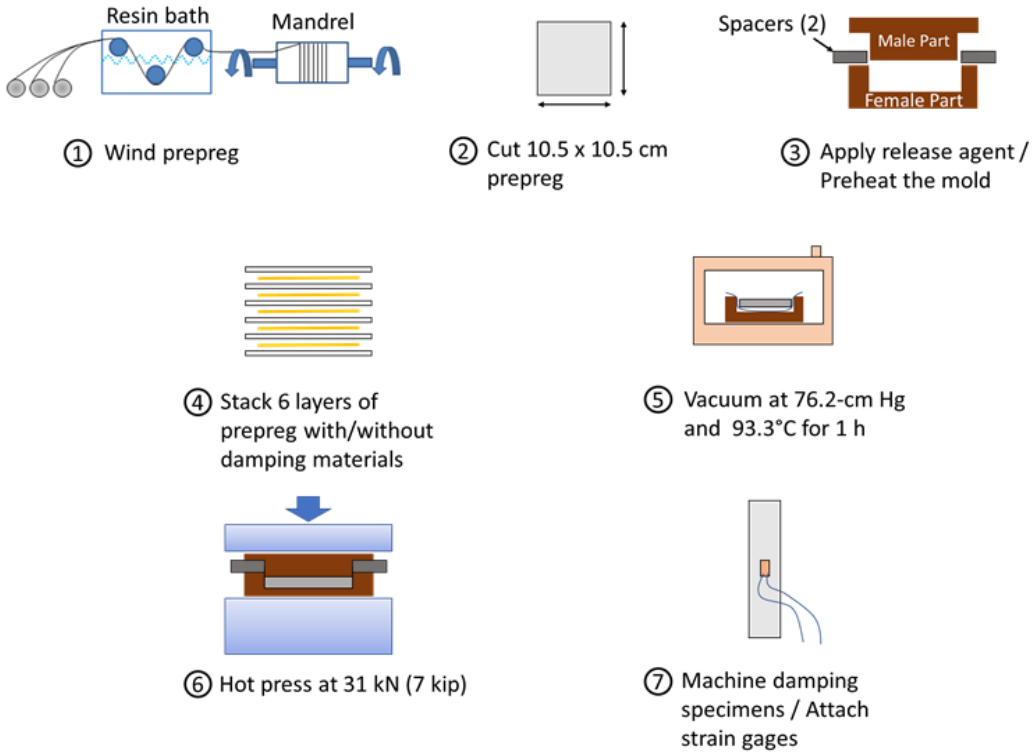

Figure 2-9: Manufacturing process for making damping specimens.

$[90]_6$, $[0]_6$, and $[0/\pm45]_s$ laminates were made with a 10.5×10.5 cm^2 two-part steel mold to make 2.54-cm-wide and 10.5-cm-long specimens, whereas $[45]_6$ in-plane shear specimens of 1.27-cm-width and 26.7-cm-length were made with a 26.7×10.5 cm^2 two-part steel mold (Figure 2-10).

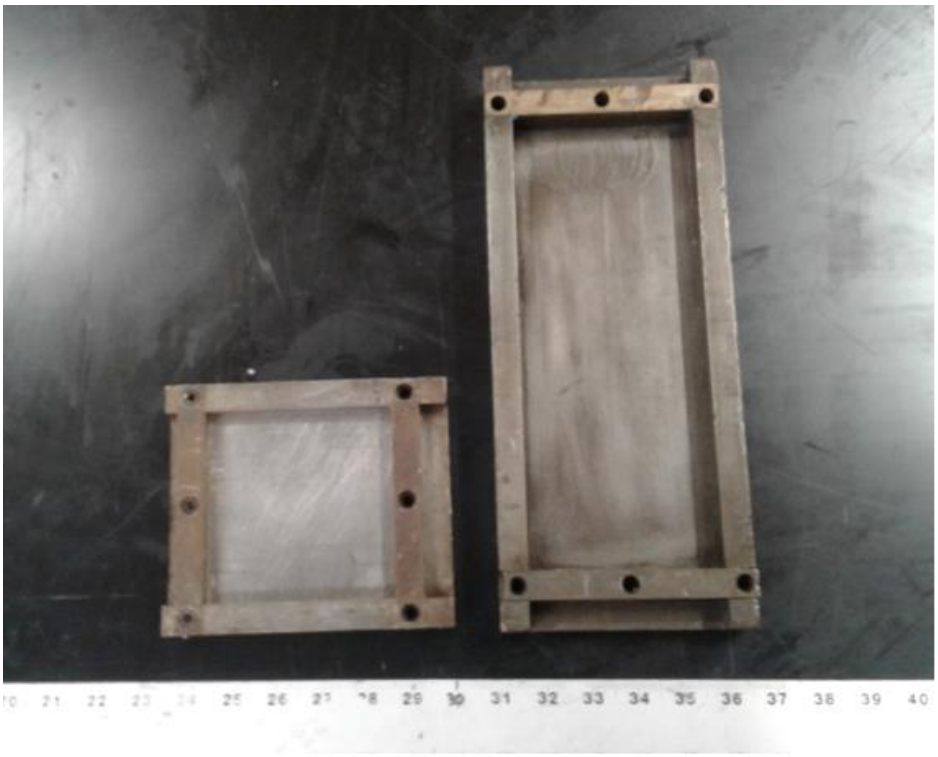

Figure 2-10: 10.5×10.5 cm^2 and 26.7×10.5 cm^2 two-part molds (ruler shows inches).

Due to extension shear coupling, 45° off-axis specimen can experience significant variation of axial stress across their thickness as well as significant shear stress in the gage section if the length of the specimen is not sufficiently higher than the width. Based on the analysis provided by Pindera and Herakovich (1986), a 1:20 width:length ratio was adopted to minimize these problems in the 45° off-axis specimens. Depending on the fiber orientation, six 10.5×10.5 cm^2 or 26.7×10.5 cm^2 sheets were cut out from the prepreg and were later stacked together with or without damping materials in the interlayer (Figure 2-11).

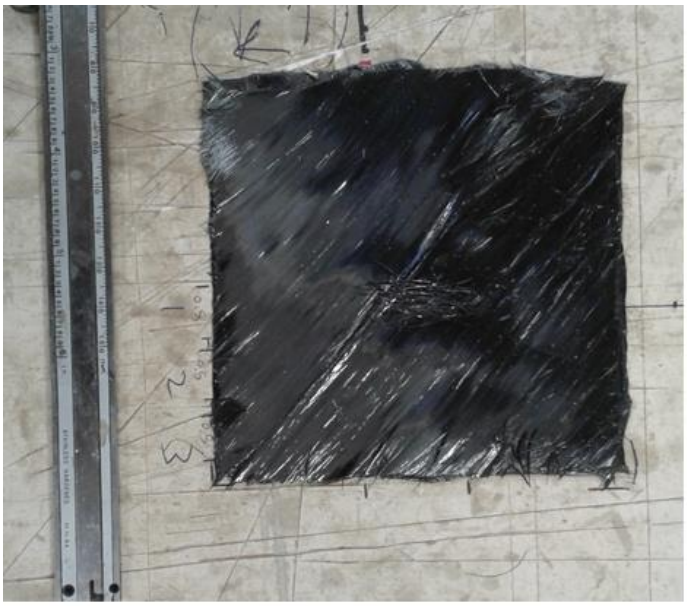

Figure 2-11: One layer of 45° prepreg for 10.5×10.5 cm^2 uncured $[0/\pm45]_s$ laminate.

The two-part steel mold was released with a releasing agent, Chemlease 41-90 EZ from Chem-Trend L.P (Howell, MI), and preheated at 71°C for an hour. Three materials were placed on the female part in the following order: Non-porous polytetrafluoroethylene (PTFE) cloth, semi-porous PTFE cloth, and uncured laminate. Vacuum was pulled at 76.2 cm-Hg and at 71°C in NAPCO 5831 vacuum oven (Thermo Fisher Scientific, Waltham, MA) for one hour in order to remove voids trapped in the uncured laminate as much as possible. In the case of the longer mold, only the uncured laminate and the PTFE cloth were placed in the vacuum chamber because the longer mold did not fit. After the vacuum procedure, another set of semi-porous and non-porous PTFE cloths was placed on the top surface of the uncured laminate, and the mold was closed with the top part (Figure 2-12).

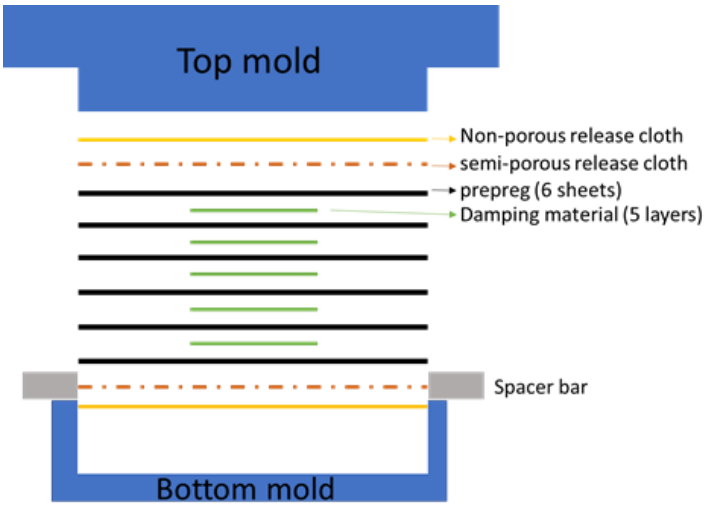

Figure 2-12: Layup of the laminate and release cloths in the mold.

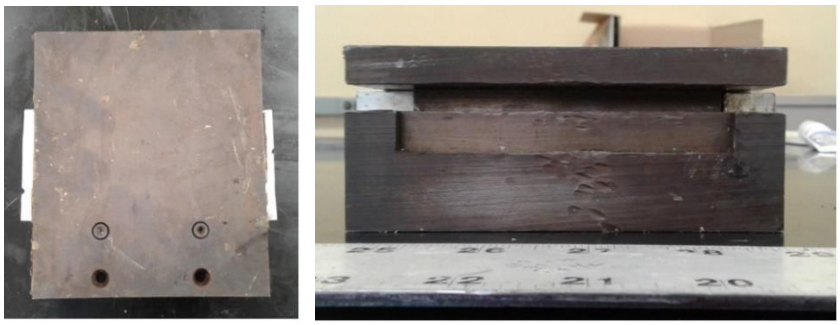

Figure 2-13: Closed mold with aluminum spacer bars in the mold halves top (left) and side (right) view.

Figure 2-14: Hot pressing the two-part mold.

The thickness of the laminate was controlled to be 2 mm by placing two aluminum spacers in between the mold halves (Figure 2-13). The laminate was cured using a hot press for one hour at 121°C and then post-cured for 3.5 hours at 177 °C (Figure 2-14). White breather was placed around the mold in order to maintain the controlled temperature. After the curing cycle, 10.5×2.54 cm^2 or 26.7×1.3 cm^2 specimen was cut with water-cooled diamond abrasive blade (Figure 2-15).

Figure 2-15: Felker 41AR 1 hp water-cooled tile saw with a diamond blade.

Table 2-2 presents the material type, stacking sequence, type of damping material, volume or weight content, type of surfactant, and material:surfactant mass ratio. The diagram of CTN yarn alignment in particular is shown in Figure 2-16. PU veil, VDP, GBP, LCBP, and SCBP were all prepared by cutting a 3.2-cm width by 3.2-cm length square patch and placing the material on each interlayer. SMA wires and CNT yarns were prepared by cutting 2.54-cm length pieces and placing the material on each interlayer. In the case of CSR and CSR-NS, the prepregs made with Kaneka MX-135 or with the combination of Kaneka MX-135 and 3M 4833 were used to manufacture c/ep laminate with CSR or CSR-NS, respectively. PZT on the other hand required a couple of additional steps. PZT powders and 862/W were mixed with the mass ratio of 1:3.85

(PZT:862/W) and was sonicated for 30 minutes at 900 W using the tip sonicator. A syringe was used to add 4 grams of the mixture in the c/ep laminate. The density, 7.95 g/cm^3, was used to obtain 0.5 vol.% (Table A-15 and Table A-16).

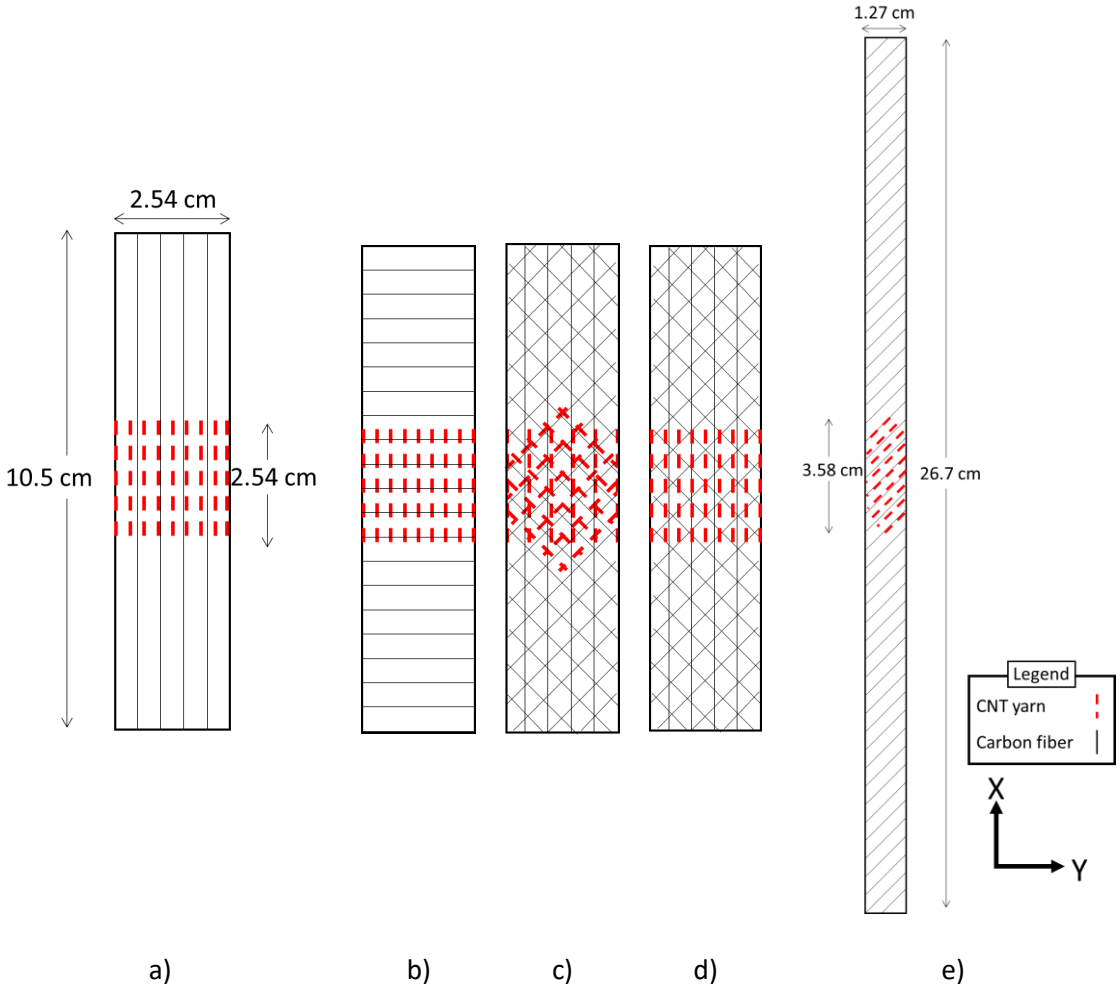

Figure 2-16: Diagram of the CNT yarn layup in a) $[0]_6$ laminate, b) $[90]_6$ laminate, c) $[0/\pm45]_s$ laminate with CNT yarns in the fiber direction, d) $[0/\pm45]_s$ laminate with CNT yarns in the loading direction, and e) $[45]_6$ laminate.

Table 2-2: Description of damping specimens.

Material Type	Laminate	Type of Damping Material	Damping Material Vol.%	Type of Surfactant	CNT: Surfactant Mass Ratio
Baseline	$[90]_6$	None	--	None	--
Baseline	$[0]_6$	None	--	None	--
Baseline	$[0]_4$	None	--	None	--
Baseline	$[45]_6$	None	--	None	--
LCBP1.3%-TX0.76	$[90]_6$	Long CNT Buckypaper	1.3%	Triton X-100	1:0.76
SCBP1.3%-TX0.76	$[90]_6$	Short CNT Buckypaper	1.3%	Triton X-100	1:0.76
SCBP1.3%-SDS0.76	$[90]_6$	Short CNT Buckypaper	1.3%	SDS	1:0.76
TX2	$[90]_6$	None	--	Triton X-100	1:2
TX4	$[90]_6$	None	--	Triton X-100	1:4
YN2.5%	$[90]_6$	CNT Yarn	2.5%	None	--
YN10%	$[90]_6$	CNT Yarn	10.0%	None	--
YN1.3%-SDS0.76	$[90]_6$	CNT Yarn	1.3%	SDS	1:0.76
YN1.3%-TX0.76	$[90]_6$	CNT Yarn	1.3%	Triton X-100	1:0.76
YN10%-TX4	$[90]_6$	CNT Yarn	10.0%	Triton X-100	1:4
YN10%-TX4	$[0/\pm45]_s$	CNT Yarn	10.0%	Triton X-100	1:4
YN10%-TX4	$[0]_6$	CNT Yarn	10.0%	Triton X-100	1:4
PU veil	$[90]_6$	Polyurethane veil	1%[2]	None	--
VDP 12.5%	$[90]_6$	Viscoelastic damper	12.5%[2]	None	--
PZT 0.5%	$[90]_6$	PZT powder	0.50%[2]	None	--
CSR 21%	$[90]_6$	CSR	21%[1]	None	--
CSR 13.3%-NS 13.3%	$[90]_6$	CSR and NS	13.3%[1] each	None	--
SMA-H 2.4%	$[90]_6$	Heat-treated NiTi SMA	2.4%[2]	None	--
GBP 6.1%	$[90]_6$	Graphene buckypaper	6.1%[2]	None	--

[1] weight percent
[2] refer to Table A-16 for the volume fraction calculation

2.5 Resin Infiltration

2.5.1 CNT Yarn

The volume content of CNT yarn (1.3%, 2.5%, and 10%) and amount of surfactant (1:0.76, 1:2, and 1:4 mass ratio of CNT:surfactant) were investigated in different ply orientations. The number of yarns required to obtain desired volume fraction was determined based on the diameter of the yarn, the bulk density of the CNT yarn provided by the manufacturer, density of CNT, and cross-sectional area of a specimen (Nanocomp Technologies, 2016). As an example, 580 pieces of yarn was required to obtain 10 vol.% CNT yarn in specimens of 2.54-cm width and 0.2-cm thickness (Equation 5). The length of the yarn was restricted to 2.54 cm due to the high cost of the CNT yarn, $4.01/meter.

$$n_{yn} = \frac{10\%\ A_{comp}}{A_{cnt}} = \frac{0.1\ w \times t}{\frac{d_{yn}^2 \pi}{4} \cdot \frac{\rho_{yn}}{\rho_{cnt}}} \tag{5}$$

where

n_{yn} = number of yarns

A_{comp} = cross-sectional area of a composite

A_{cnt} = cross-sectional area of CNT in one yarn

w = width = 2.54 cm

t = thickness = 0.2 cm

d_{yn} = diameter of CNT yarn = 0.0150 cm

ρ_{cnt} = density of CNT = 1.6 g/cm^3 (Sugime et al. 2013)

ρ_{yn} = density of CNT yarn =0.8 g/cm^3 (Nanocomp Technologies, 2016)

ρ_{cnt} is the assumed density of a MWCNT with sealed ends, as if epoxy resin did not infiltrate the empty space in between each wall of the MWCNT and also the inside of the innermost wall of the MWCNT. The volume content of the CNTs in the CNT yarn was calculated to be 50% by dividing ρ_{yn} by ρ_{cnt}. The rest of the content was considered as empty space between adjacent MWCNTs that could prospectively be filled with resin. The CNT yarns were impregnated in the mixture of resin and surfactant. When 50 wt.% and 25 wt.% of 862W were surfactants, the mixture ultimately led to 1:4 and 1:2 of CNT:surfactant, respectively (Figure 2-17). An example of the calculation can be found in Table A-1.

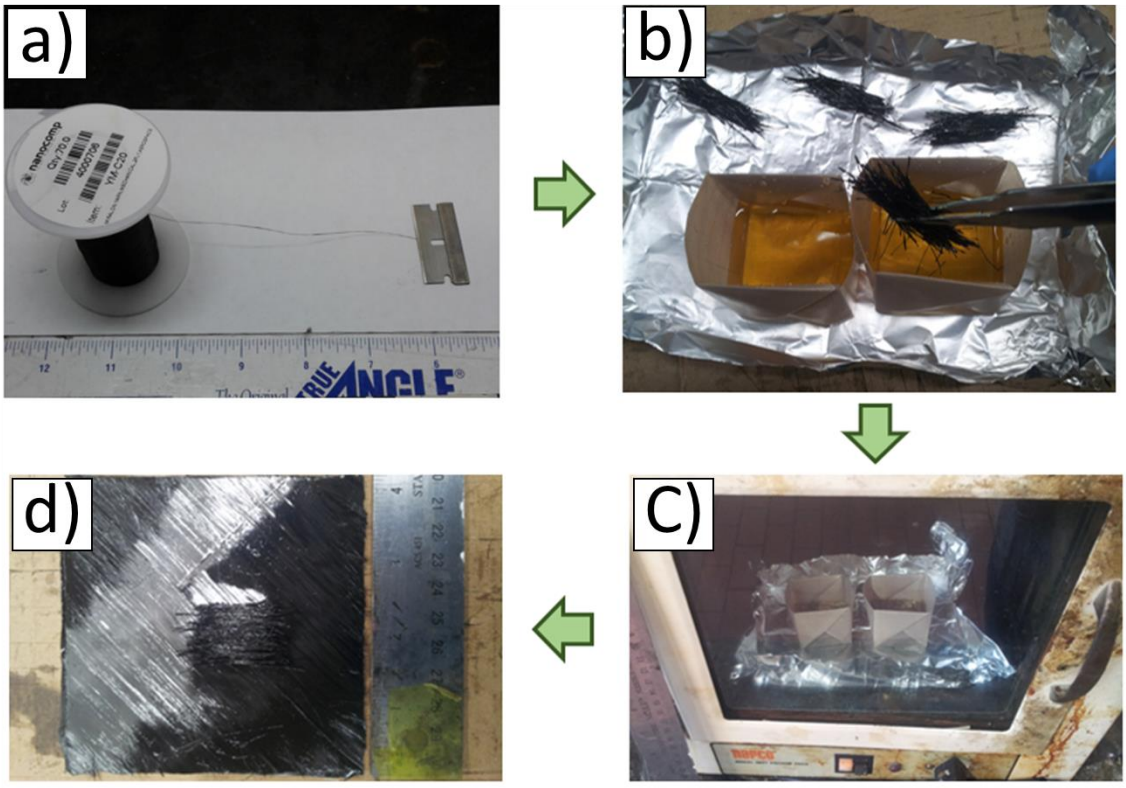

Figure 2-17: Procedure for preparing CNT yarns: a) Cutting CNT yarns with a razor blade, b) mixing CNT yarn, 862/W, and surfactant c) impregnating CNT yarns at elevated temperature and pressure d) placing CNT yarns on a prepreg.

A NAPCO 5831 vacuum oven was used to impregnate CNT yarns in the mixture at an elevated temperature of 93°C and 76.2 cm-Hg vacuum for 1 hour. After distributing impregnated CNT yarns on the prepregs when manufacturing c/ep plates, the weight of a PTFE container or 100 ml beaker full of mixture and CNT yarns before and after was used to estimate the final mass of the surfactant transferred onto prepregs.

2.5.2 Buckypaper

Buckypaper of 20 gsm areal weight was inserted in the interlayer of C/E laminate with or without surfactant to evaluate its effect on damping performance. In each interlayer, a patch of 3.8 × 3.8 cm^2 buckypaper was placed on 10.5 ×10.5 cm^2 prepreg to conserve the expensive material. CNT to surfactant mass ratios of 1:0.76 was studied to observe the effect of surfactants on the damping behavior. Due to the high concentration and viscosity of surfactants, the amount of acetone corresponding to the CNT to surfactant mass ratio was mixed with acetone and buckypaper in a PTFE container. The mixture stayed in the container for 24 hours at room temperature until the acetone evaporated. This surfactant-treated buckypaper was then inserted in the c/ep laminate as a damping material during the lamination procedure.

2.5.3 Specimens for Volume Fraction Analysis

For constituent volume fraction analysis, a $[90]_6$ baseline laminate was potted with EPON 862 and Jeffamine T-403 epoxy system in an Allied 2.54-cm-diameter two-part mold (Figure 2-18). The mass ratio of the resin mixture was 100:42 (EPON 862:Jeffamine T-403), and the resin was cured for 24 hours at room temperature. A MetPrep 3™ Grinder/Polisher at the Materials

Characterization Laboratory at Penn State (Figure 2-19) was used to grind and polish the surface according to the procedure in Table 2-3.

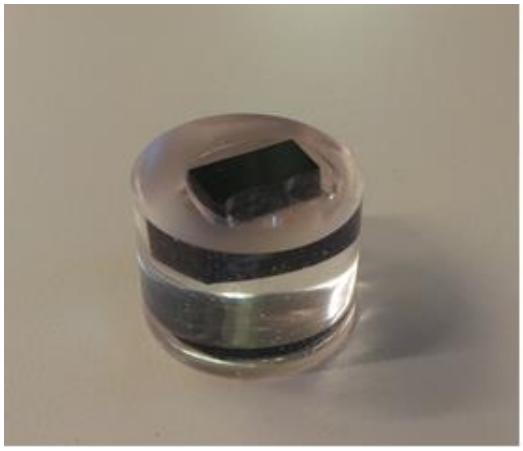

Figure 2-18: 2.54-cm diameter potted sample for volume fraction analysis.

Figure 2-19: MetPrep 3™ Grinding/polishing setup.

Table 2-3: Procedure for grinding and polishing specimens.

Abrasive size (P-grading)	Carrier	Sample speed (RPM)	Platen speed (RPM)	Force (lbf)	Time (min.)	# cycles
320	water	60	120	1	2	Until Flat
800	water	60	120	1	2	3
1200	water	60	150	1	2	3
2400	water	80	150	2	2	3
4000	water	80	150	2	2	3
3 μm poly. diamond (white pad)	glycol susp.	80	300	2	3	2
1 μm poly. diamond (white pad)	glycol susp.	80	300	2	3	2

2.6 Tensile Strength Specimen

$[0/\pm45]_s$ laminates with or without damping materials were tested for tensile strength in order the observe the effect of CNT and surfactant on tensile strength. 10.5×10.5 cm^2 mold was used to manufacture a set of three baseline as well as the CNT specimens of 1.27 cm-width and 10.5 cm-long. Three hundred 2.54 cm-long CNT yarns were impregnated with resin and Triton X-100 to get 1:4 mass ratio by following the procedure mentioned in the previous sections.

2.7 Pullout Specimen

CNT yarn pullout specimens were fabricated in a silicone mold using a needle and 862/W with TX in order to investigate the critical shear stress of the yarn (Figure 2-20). The first step to make the specimens was to insert CNT yarns through the silicone mold after releasing the mold with Chemlease 41-90 EZ. The yarn passed through the eye of the needle, forming a tail. Then

the needle was passed through the two walls of the silicone mold. Once the needle exited the walls, the tail of the yarn was slowly pulled, in the end leaving one line of yarn traveling across the mold. After three yarns were inserted in the mold, specimens underwent the curing procedure described in Figure 2-20. A pre-vacuumed resin mixture of equal amount of 862/W and Triton X-100 in a 100 ml beaker was poured into the silicone mold and then the yarns were impregnated with the resin mixture for one hour at 76.2-cm Hg vacuum and 93°C (Table A-1). The pullout specimens were then cured at 121°C for one hour followed by 177°C for 3.5 hours in a mechanical convection oven. After the curing process, yarns were gently taken out from the soft silicone mold by deforming the walls to provide more space in between the epoxy and the mold. Figure 2-21 shows the image of cured pullout specimens. Water-assisted diamond saw blade and water-assisted hand grinder were used to cut three specimens and to grind off the tail of the yarn, respectively.

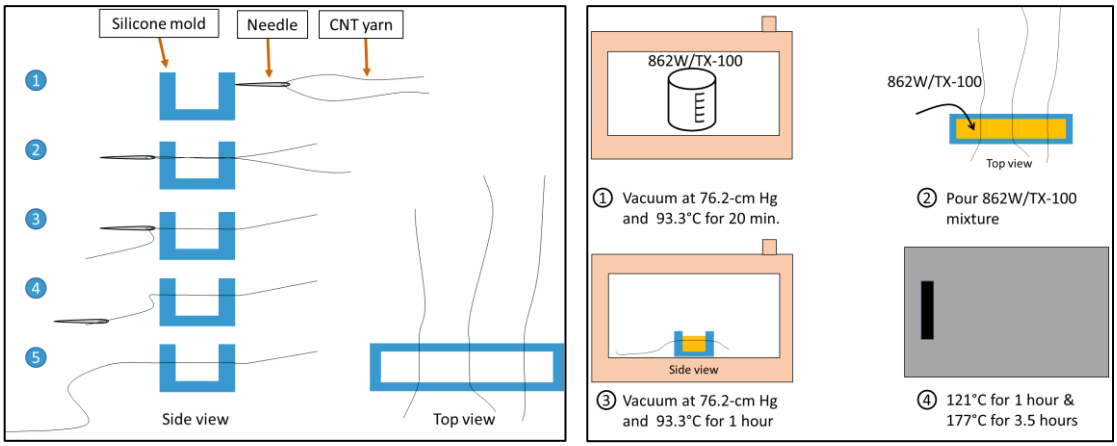

Figure 2-20: Insertion of CNT yarn in a silicone mold (left) and curing procedure (right).

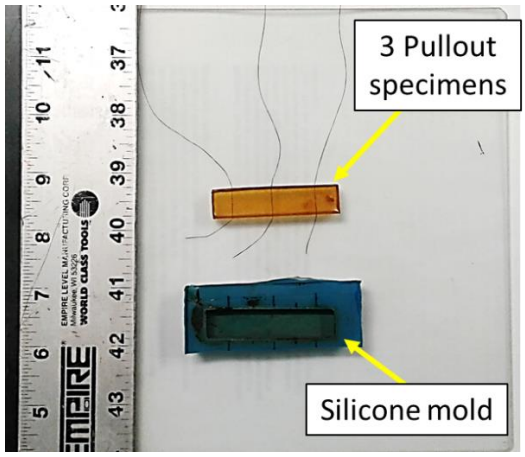

Figure 2-21: Three CNT yarn pullout specimens taken out from the silicone mold after post-curing. Ruler is in inches.

Chapter 3

Test Methods

This chapter is divided into four sections in which checking the quality of manufactured specimens and method of tests as well as the necessary preparation protocols are explained. Section 3.1 describes how to process image analysis on specimens for volume content. Section 3.2 explains the damping test method and test conditions in detail. Section 3.3 explains the tensile strength test. Section 3.4 explains how to perform pullout test for critical shear stress of CNT yarns.

3.1 Specimen Quality Check

3.1.1 Field Emission Scanning Electron Microscopy

FEI Nova NanoSEM 630 Field emission scanning electron microscopy (FESEM) was used to evaluate the degree of resin infiltration into CNT yarn and also to determine the aspect

ratio of CNTs for CNT yarn and buckypapers. Iridium was sputtered on specimens for 30 seconds with EMS 150T Plus Turbomolecular Pumped Coater (Hatfield, PA) in order to increase the conductivity of samples and therefore prevent charging when high energy electrons bombard the surface of samples. Both instruments are located in the Materials Characterization Lab (MCL) at Penn State.

3.1.2 Optical Microscopy

An Olympus MX50 microscope located at the Penn State Materials Characterization Laboratory as used to study the volume fraction analysis of c/ep specimens. Thirty images of 500× magnification were analyzed with the "ImageJ" software program, which can be download for free online. Analyzing images of higher magnification such as 5000× leads to more accurate results due to shaper borders between materials. However, the volume fractions did not vary significantly when the two magnifications mentioned above were compared. The comparison of 500× and 5000× magnification results is shown in Table A-2 and Figure A-1.

A couple of steps were necessary in order to analyze the fiber, matrix, and void, all of which made up the content of c/ep baseline material (Figure 3-1). Unless the images were captured automatically in grayscale, they had to be converted to grayscale, which ImageJ could take care of as well by selecting "8-bit" in "Image → Type → 8-bit" (Figure 3-2a). To measure the volume content, "Threshold" was selected in "Image → Adjust → Threshold" as described in Figure 3-2b. Void volume fraction (V_v) was measured by first setting "Min" at 0 and "Max" at a value which highlighted only the black regions in the image (Figure 3-3). The percentage shown under the threshold window after clicking "Apply" was the void volume content. Fiber volume fraction (V_f) was measured similar to V_v, except that "Max" was set at the maximum value and "Min" at the value which highlighted only the fibers (Figure 3-4). Additional ImageJ analysis was

not necessary to measure the matrix volume fraction (V_m) because the subtraction of V_f and V_v from 100% gave V_m. This analysis was performed on 30 images, after which the average and standard deviation of the volume contents were calculated. The volume fraction analysis could not be performed properly on the specimens containing CNTs due to the fact that the yarns were not spread out uniformly. Without the uniform distribution, V_f and V_m could not be analyzed accurately. As a result, only the V_v was measured in the case of the specimens containing CNTs.

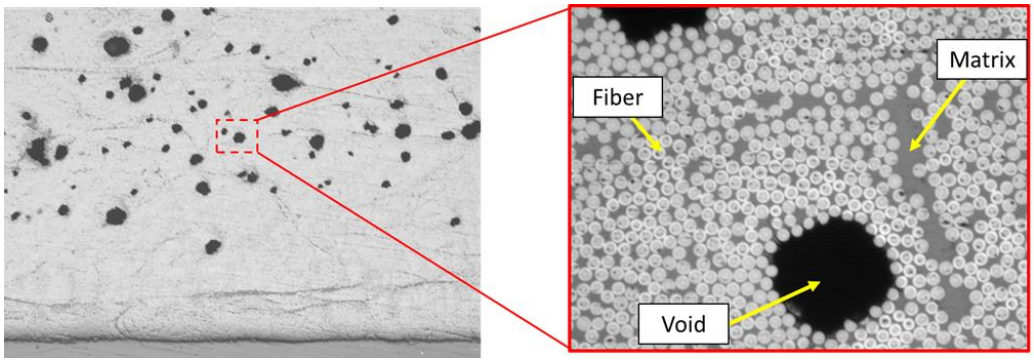

Figure 3-1: Representative photomicrograph of a poorly manufactured c/ep specimen that has large voids.

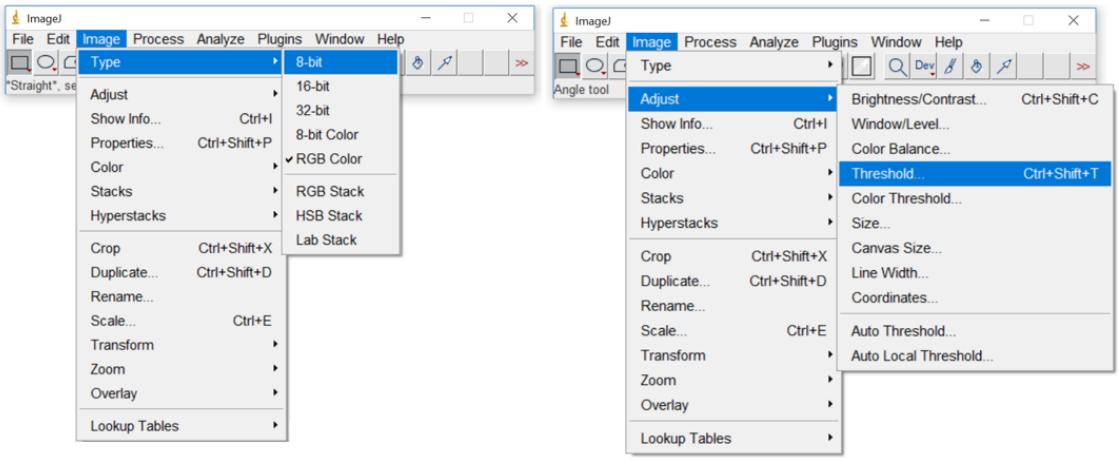

Figure 3-2: Converting the type of image to 8-bit grayscale (left) selecting threshold (right).

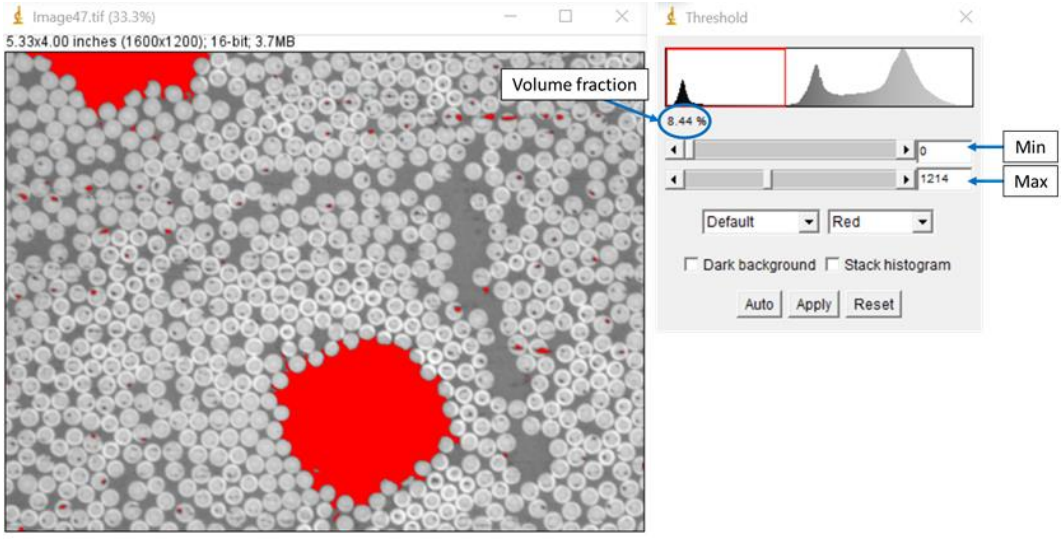

Figure 3-3: Highlighting voids using ImageJ.

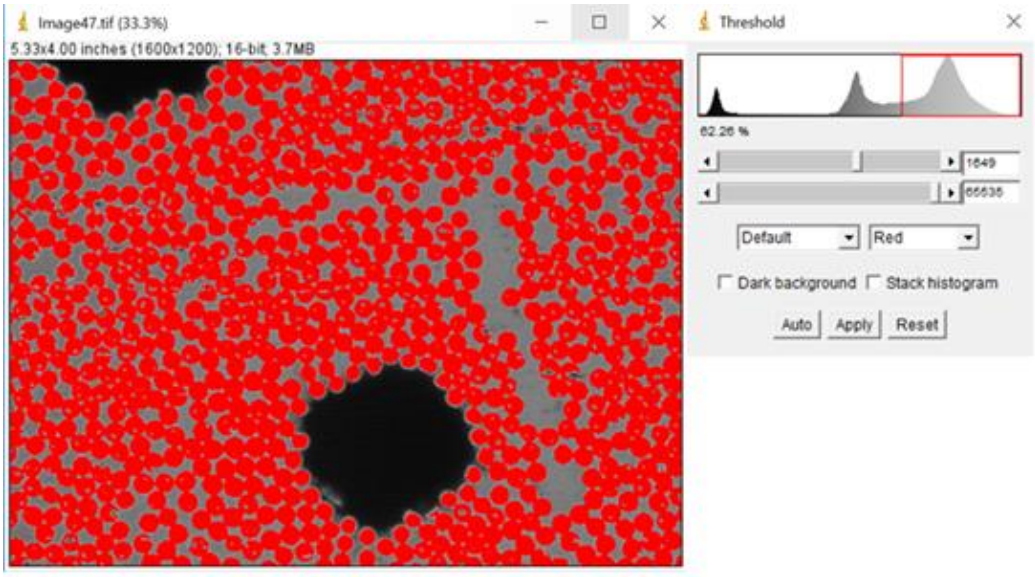

Figure 3-4: Highlighting carbon fibers using ImageJ.

3.2 Damping test

In this section, the damping test method is explained. The damping test setup, test procedures, data analysis, limitations of the test setup, and conditions under which damping test was performed are described in detail.

3.2.1 Overview of Test Setup

Figure 3-5 shows the Model 810 MTS servo-hydraulic load frame with 49 kN (11 kip) load cell and 24 kN (5.5 kip) hydraulic grips which was used not only to measure the dynamic properties in tension but also to apply fatigue loading cycles to certain specimens.

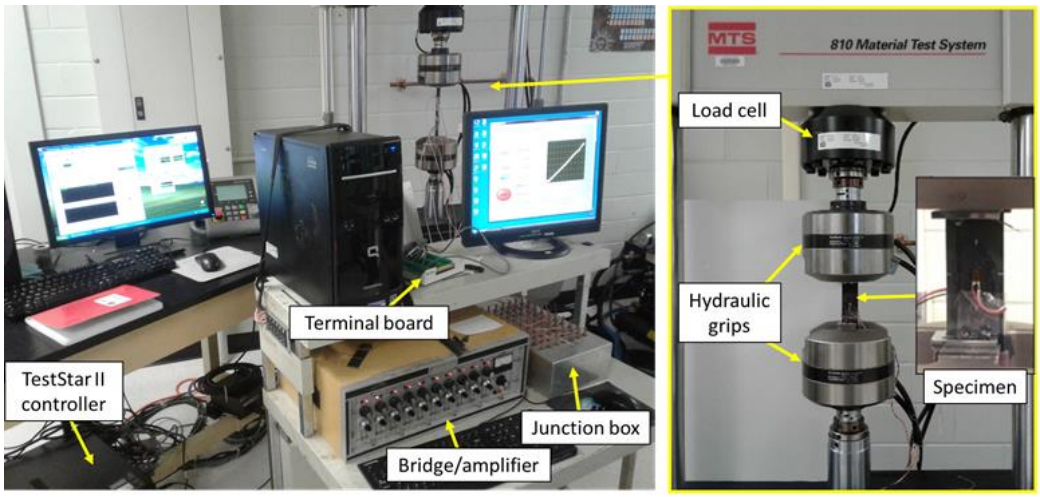

Figure 3-5: 810 MTS machine damping test setup.

Tension testing was selected over bend testing in order to attain a homogeneous strain field in the gage section and therefore properly observe the effects of strain excursions on damping, as the literature suggests that damping of materials containing CNTs varies in a non-linear manner with strain. Analog load and strain signals were collected at the sampling frequency of 150 Hz from the load cell and external strain conditioning equipment, including a Model 2100 Wheatstone bridge/amplifier (Vishay Measurements Group, Wendell, NC) and NI SCB-68 pin terminal board (National Instruments, Austin, TX) (Figure 3-6). The “7 channel voltage” VI of LabVIEW was used to collect the output signals through the NI PCI-6220 data acquisition system (DAQ) card (National Instruments, Austin, TX). Several preliminary investigations, described next, were carried out to establish the best method of obtaining the dynamic properties of c/ep laminate.

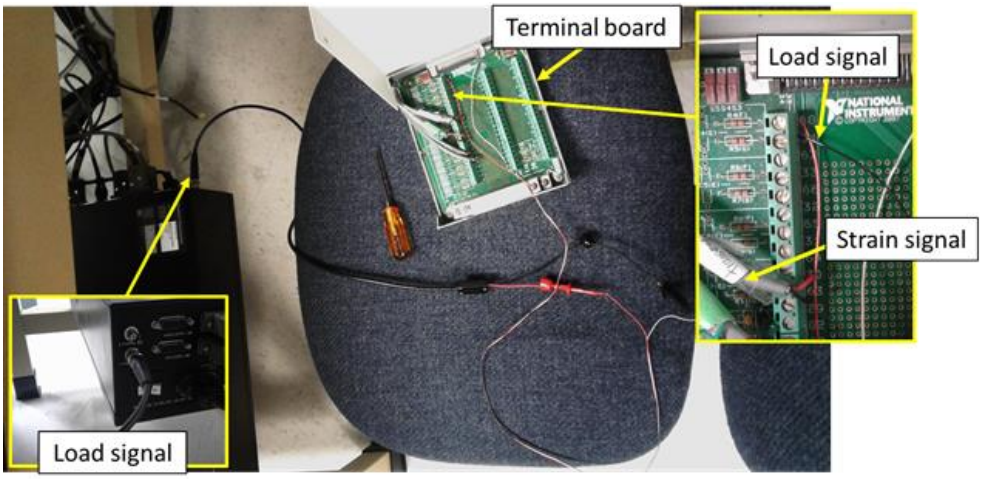

Figure 3-6: Load signal connection.

3.2.2 Method of Collecting Strain Signal

Among various strain measurement techniques, a clip-on extensometer and unidirectional strain gage were evaluated to determine which technique would give a lower standard deviation in the dynamic properties. In this section, the procedures and results for three different strain measurement techniques are provided.

For the two extensometer techniques, a 13-mm clip-on MTS extensometer and V-notched tabs bonded to a specimen with either soft silicone adhesive from General Electric (Boston, MA) or M-Bond 200 adhesive (cyanoacrylate), purchased from the Vishay Measurements Group were used. Figure 3-7 shows how two V-notched tabs were bonded to the specimen.

Figure 3-7: Bonding extensometer tabs (left) and aligning the tabs with the extensometer (right).

The surface of specimens was prepared with Scotch-Brite abrasive and acetone in order to smooth out the surface and remove debris for stronger adhesion. After either of the adhesives was applied on the specimen, and the tabs were positioned by pressing the two knife edges of the extensometer into the V-notches. The extensometer was carefully removed from the tabs and then the adhesive was cured.

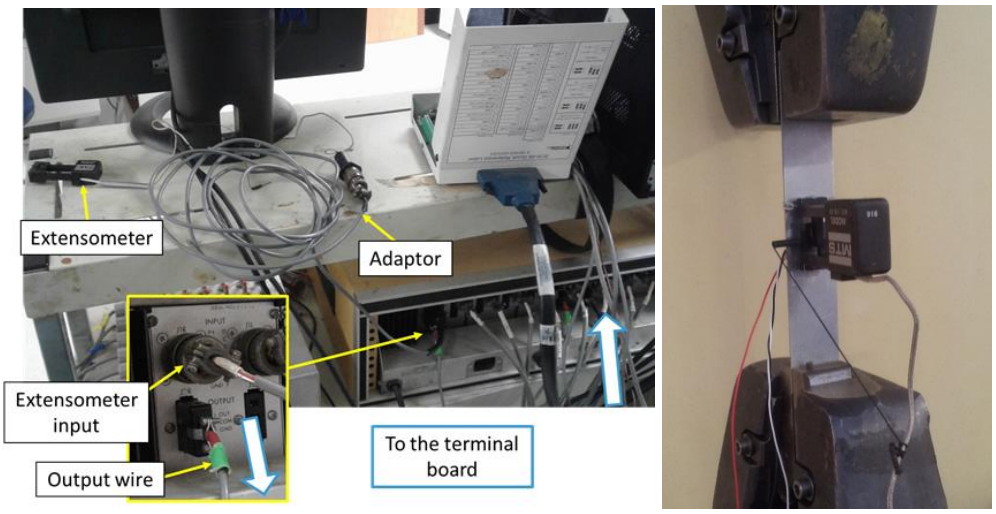

Figure 3-8: Extensometer connection.

With the specimen ready for the damping test, the extensometer had to be calibrated. An adaptor was used to connect extensometer to one channel of the bridge/amplifier (Figure 3-8). The course gain setting was set to "×200" and the excitation voltage of the channel was maximized to 12 V by turning the "BRIDGE EXCIT" knob, right above the "EXCIT ON" switch, with a flat screwdriver not only to increase the sensitivity of the extensometer but also to increase the signal to noise ratio (Figure 3-9).

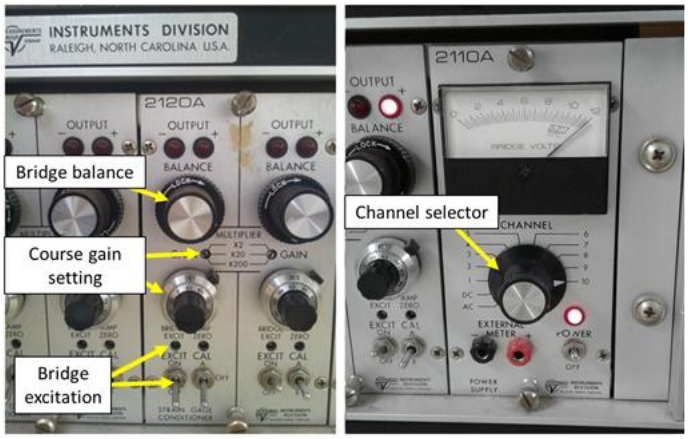

Figure 3-9: Bridge/amplifier (left), Power supply (right)

The signal was read through the three-prong output wire connecting the bridge/amplifier and the terminal board for the LabVIEW data acquisition board. A caliper was used to calibrate the extensometer by taking the linear relationship between the voltage signal and the distance of the two knife edges of the extensometer. Figure 3-10 shows an example of the unit conversion from voltage to length.

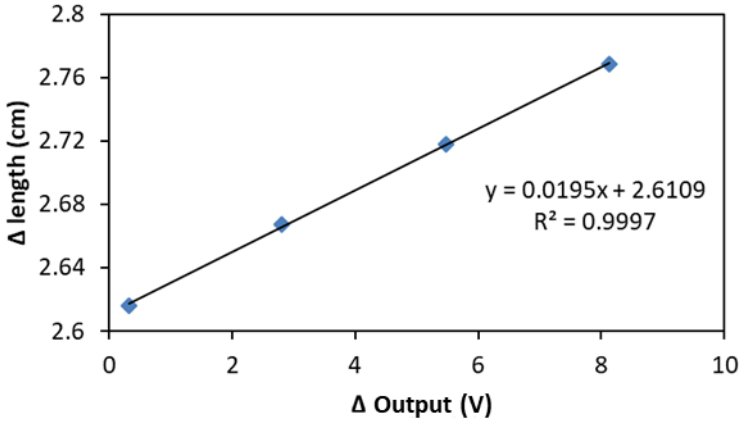

Figure 3-10: Calibration chart for extensometer.

As for the strain gage technique, unidirectional strain gage, CEA-06-125UN-120 (Vishay Measurements Group, Wendell, NC) or 45° triaxial rectangular rosette, CEA-06-062UR-120

(Vishay Measurements Group, Wendell, NC), for shear dynamic properties, was used to collect the strain signal. The strain gage was used only on one side for the preliminary investigations where different strain measurement techniques were compared. However, the strain gage was used on the front and the back side afterwards in order to eliminate the bending. The detailed instruction of strain gage attachment presented by the Vishay Measurements Group was followed to attach strain gages on the front and back of specimens (Micro-Measurements, 2011a; Micro-Measurements 2018). The gage section of the specimen was cleaned with acetone to remove grease and contaminants. Acidic "Conditioner A" and Scotch-Brite abrasive were used to smooth out the surface. In order balance the alkalinity back to 7 pH to create the optimal condition for the M-200 adhesive, "Neutralizer 5A" was applied on the surface and was wiped after with Kimtech wipes. A layout of a crossed line was drawn on a specimen with a marker and a ruler so that strain gages could be positioned and aligned in the loading direction. After placing strain gages on a clean flat glass plate with a tweezer, PCT installation tape was used to tape the shiny surface with the two terminals. The tape was peeled from the glass plate and placed on the specimen so that the strain gage is aligned according to the layout line. With the tape peeled half-way through so that the back of the strain gage is exposed, blue color M-Bond 200 catalyst was applied on the strain gage as well as on the surface of the specimen, allowing it to evaporate for 5 minutes. Next, a drop of M-200 adhesive applied at the junction of tape and specimen. The half of the tape was applied back onto the tape. The strain gage section was then pressed firmly with a thumb for one to two minutes until the adhesive cured. The tape was then carefully peeled after which a strip of 326-DFV solder wire was soldered onto the strain gage. White and black wires twisted together on one terminal and red wire on the other terminal were soldered with 361A-20R-25 solder (Vishay Measurements Group, Wendell, NC).

With the prepared specimen, the wires were connected to the DAQ system. Red, white, and black wires were connected to P+, S-, and D120 pins of one of the channels in the junction box, respectively (Figure 3-11).

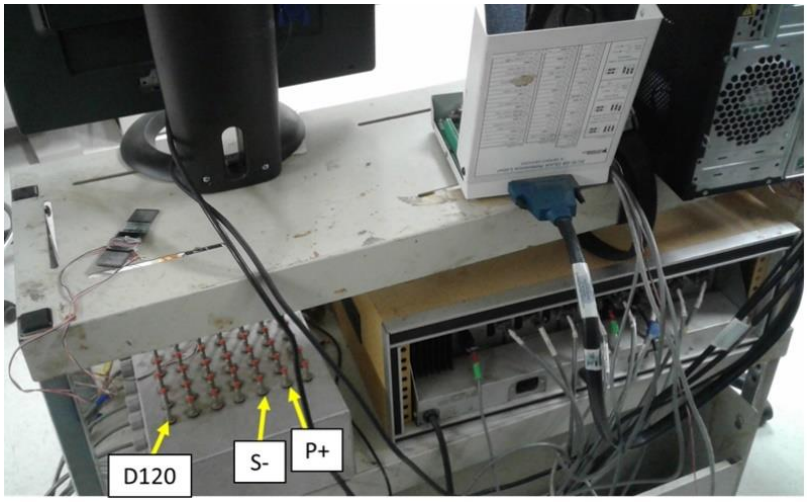

Figure 3-11: strain gage connection.

The channel was then connected to the bridge/amplifier and the output of the bridge/amplifier was connected to the terminal board for the LabVIEW DAQ card. The excitation voltage applied to the Wheatstone bridge and the course gain setting were set at 2 V and ×200. The output of the strain gages was calibrated so that one volt equaled 1000 με.

With the procedures mentioned in the following two sub-sections, the phase difference between the load and the strain signals collected from the three methods, the extensometer with cyanoacrylate (Exten. CA), the extensometer with silicone adhesive (Exten. Silicone), and the strain gage, were compared using three materials: 862/W (862W), polyurethane (PU), and aluminum (Al). It was found that the strain gage showed the lowest standard deviation of four repetitions of the damping test in all three materials (Figure 3-12). The quantitative values are found in Table A-3. Based on these results, the strain gage was selected as the strain measurement technique for the remainder of the damping tests in this investigation.

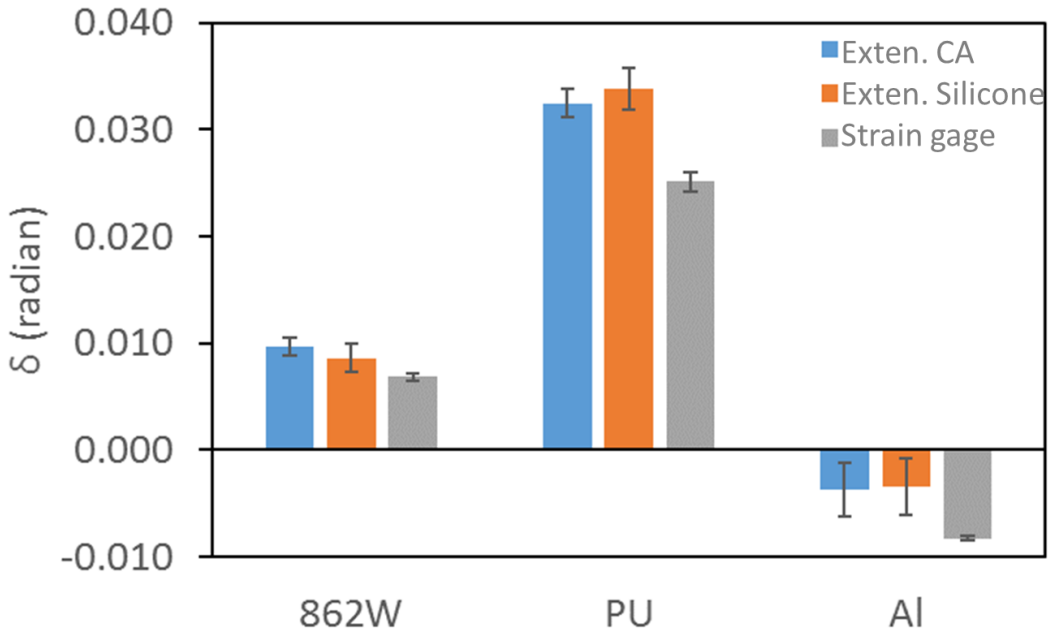

Figure 3-12: Comparing the average and the standard deviation of four phase difference measurements using different strain measurement technique.

3.2.3 Collection and Preliminary Process of Raw Data

In this section, steps for conducting the damping test and processing the raw data in Microsoft Excel are explained. With the signal measurements prepared and the MTS machine turned on in displacement control, the top part of the specimen, wrapped with the 1-inch wide 100 grit aluminum oxide sanding roll (McMaster-Carr, Elmhurst, IL) facing the specimen, was gripped with the top hydraulic grip (Figure 3-13).

Figure 3-13: Specimen gripped with sandpaper in the top grip.

The load and the strain signals should be balanced close to zero at this point since force was not applied. While leaving the bottom grip open, the "7 channel voltage" VI was turned on to collect the signals at the acquisition rate of 150 Hz (Figure 3-14).

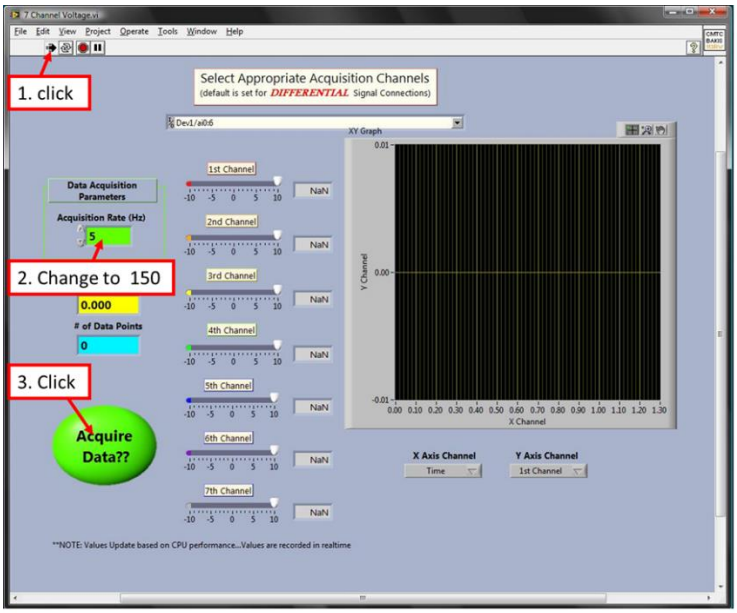

Figure 3-14: "7 channel voltage" VI.

The bottom part of the specimen was also wrapped with the sanding roll and then gripped, after which the grip pressure was increased to 5 MPa for aluminum and $[90]_6$ baseline laminate, and 14 MPa for 0° and multi-directional specimens (Figure 3-15).

Figure 3-15: Pressure gauge of the MTS machine at 5 MPa.

Some amount of tensile or compressive strain were expected as a result of straightening of specimens when gripped since they could not be manufactured perfectly straight. Then the MTS programmed procedure of the damping test was run (Figure 3-16).

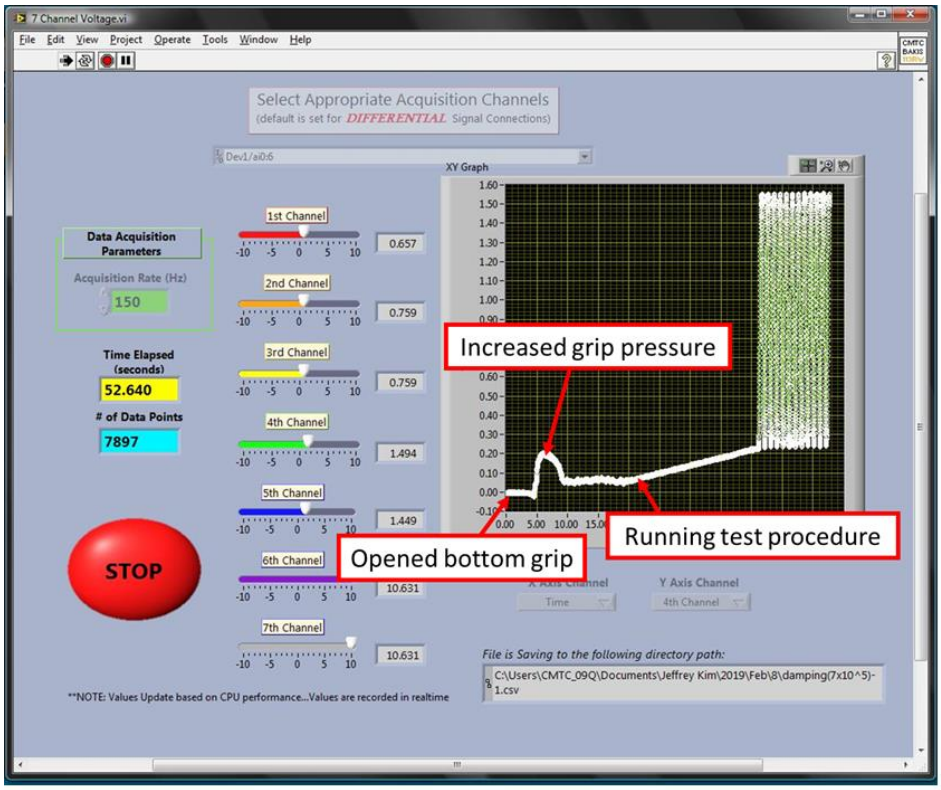

Figure 3-16: Example of collecting signals using the Labview VI.

The typical procedure was that there was an initial steady ramp in the beginning in order to raise the mean, followed by 40 cycles of sinusoidal load in tension-tension, preventing the specimen from experiencing compression. Once the VI generated an Excel file with the raw data, the first data point of the signals, which should be closer to zero since the strain was balanced to zero before the specimen is gripped, was used as the reference and therefore subtracted from the rest of the data points. The initial ramp was deleted so that only the cyclic portion was left in the excel sheet. After averaging the two strain signals, which eliminated the potential bending, the load and strain voltage signals were converted to stress and strain, respectively: 1 V equals 1000 με and the default unit conversion of 10 V equals 11240 lbf, found in the "Station Manager" of the MTS software, were used to make the conversion (Figure 3-17).

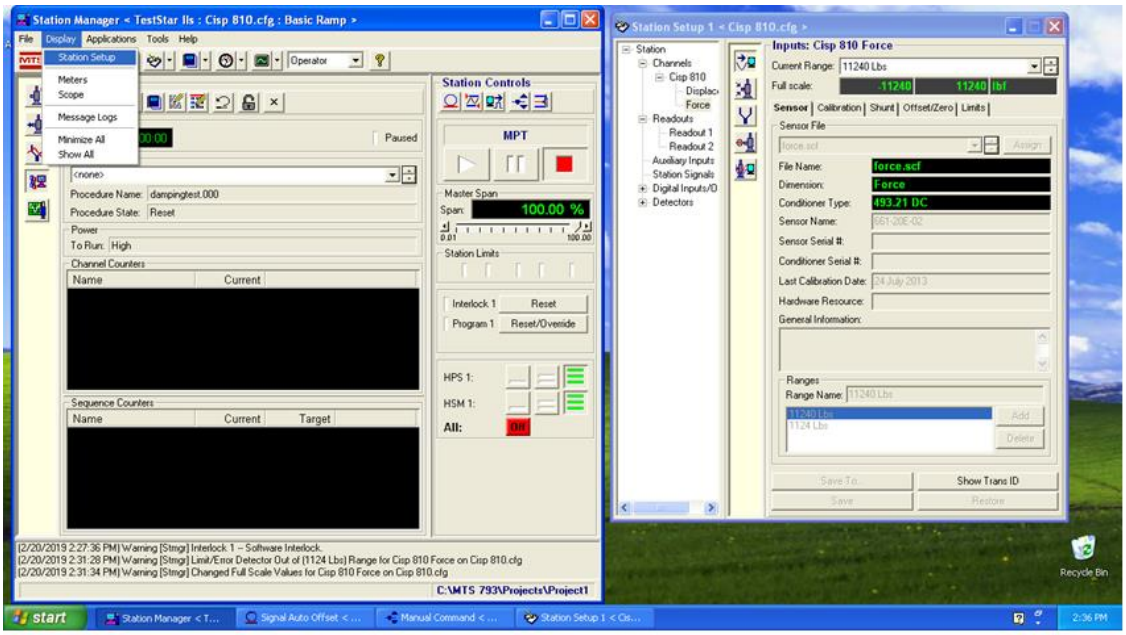

Figure 3-17: Station Manager showing voltage conversion.

3.2.4 Damping Data Analysis

A MATLAB code was programmed to analyze the raw data for obtaining the dynamic properties (Appendix B). The flow chart of processing data signals to determine the dynamic properties, tan δ, E', and E'', is shown in Figure 3-18. The dynamic properties were obtained from the phase angles and amplitudes of the stress and strain signals collected in time domain (Step 1). A fast Fourier transform (FFT) was used to convert the time domain of each signal into frequency domain from which the fundamental frequency, corresponding to the test frequency (1 Hz unless otherwise mentioned), was collected (Step 2). The phase difference between the two signals were determined by taking the difference between the phase angle of stress and strain signals (Step 3). The phase difference contained an inherent equipment phase lag that had to be taken into account. Therefore, each specimen was calibrated with the phase difference of 6061-T6 aluminum specimen (δ_{al_raw}) collected from the test setup and the reference value (δ_{al_ref}) of

0.00197 radians from Bhagat et al. 1998 (Step 4). With the calibrated phase difference (δ_{cal}) and the complex modulus obtained by ratio of the stress and strain amplitudes, tan δ, E', and E'' were determined as represented in Step 5. It must be noted that δ_{al_raw} is dependent on the test frequency. For example, δ_{al_raw} is about -0.0077 at 1 Hz but -0.0353 at 5 Hz.

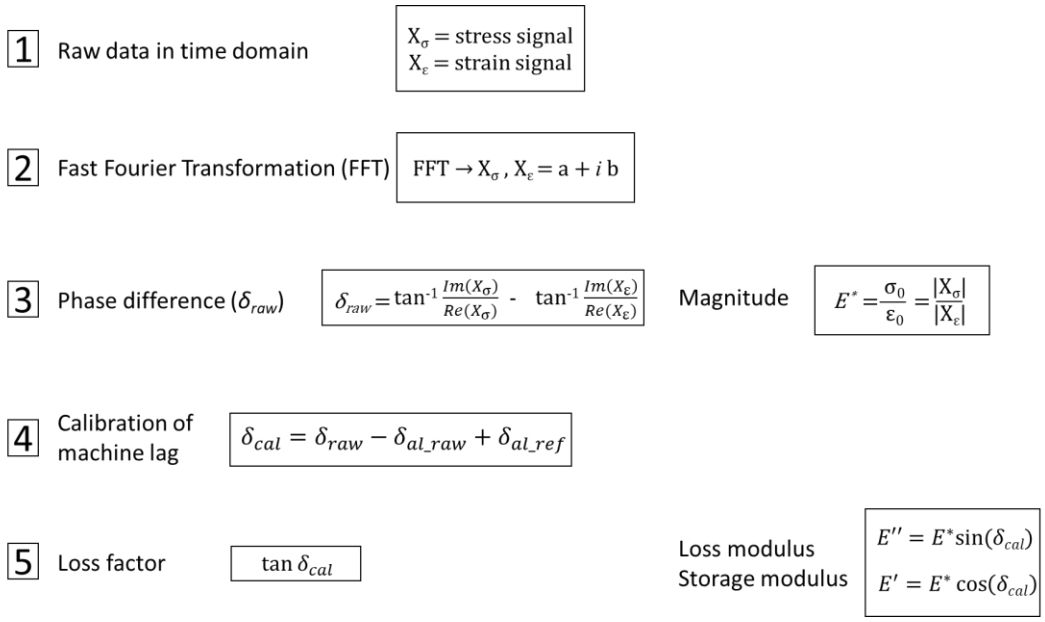

Figure 3-18: Diagram describing how to calculate the dynamic properties.

Different from axial dynamic properties, the in-plane shear dynamic properties were obtained from 45° off-axis specimens with the 45° triaxial rectangular rosette, of which the transverse sensitivity was taken into account after transforming the normal strain in three directions to shear strain and then averaging the front and back shear strains. The following equations were used to take into account the transverse sensitivity (Micro-Measurements, 2011b),

$$\varepsilon_{0^\circ} = \frac{1 - \nu_0 K_t}{1 - K_t^2}(\hat{\varepsilon_{0^\circ}} - K_t \hat{\varepsilon_{90^\circ}}) \quad (6)$$

$$\varepsilon_{45^\circ} = \frac{1 - \nu_0 K_t}{1 - K_t^2}(\hat{\varepsilon_{45^\circ}} - K_t(\hat{\varepsilon_{0^\circ}} + \hat{\varepsilon_{90^\circ}} - \hat{\varepsilon_{45^\circ}}) \quad (7)$$

$$\varepsilon_{90^\circ} = \frac{1 - \nu_0 K_t}{1 - K_t^2}\left(\hat{\varepsilon}_{90^\circ} - K_t \hat{\varepsilon}_{0^\circ}\right) \quad (8)$$

where

K_t= transverse sensitivity coefficient

$\hat{\varepsilon}_{90^\circ}$ = 90° strain gage before correction

$\hat{\varepsilon}_{0^\circ}$ = 0° strain gage before correction

$\hat{\varepsilon}_{45^\circ}$ = 45° strain gage before correction

ν_0 = 0.285 (Poisson's ratio of the material used by the manufacturer to calibrate the lot of gages)

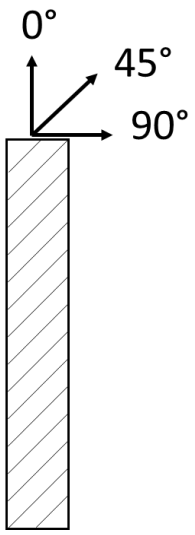

Figure 3-19: Diagram representing the direction of 0°, 45°, and 90° on the 45° lamina.

The following equations were then used to transform the three normal strains as well as the normal stress applied into shear strain and stress (Chamis and Sinclair 1977),

$$\tau_{12} = \frac{1}{2}\sigma_{cxx} \sin 2\theta \quad (9)$$

$$\varepsilon_{cxy} = -\varepsilon_{0^\circ} + 2\varepsilon_{c90^\circ} - \varepsilon_{45^\circ} \quad (10)$$

$$\gamma_{12} = (\varepsilon_{90^\circ} - \varepsilon_{0^\circ}) \sin 2\theta + \varepsilon_{cxy} \cos 2\theta \quad (11)$$

where σ_{cxx} is the applied normal stress, τ_{12} is the shear stress parallel to the fibers, γ_{12} is the shear strain parallel to the fibers, and θ is the fiber angle, which is 45° in this case. The two shear strain measurements from the front and back rosettes were then averaged.

3.2.5 Limitation and Error

Test variability, material variability, and the minimum load and strain needed to get the consistent dynamic properties were investigated for proper test design. In these variation tests, three repetitions of damping test were conducted on three samples of each unidirectional baseline laminate – $[0]_6$, $[45]_6$, and $[90]_6$ – to observe the variations on the three dynamic properties. The damping test was conducted at various load amplitudes from 22 N (5 lbf) to 254 N (57 lbf) on the aluminum calibration specimen, of which the damping is assumed to be independent of strain amplitude, in order to observe the point at which phase difference would become consistent.

3.2.6 Damping Conditions

As damping properties of materials are dependent on various factors, damping test under different conditions was necessary to observe stable behaviors in order for damping materials to be considered as a serious candidate. Therefore, the effect of strain, fatigue and temperature on the dynamic properties of $[0/\pm45]_s$ baseline and YN10%-TX4 laminates were investigated. The frequency of the damping test remained at 1 Hz throughout the study.

3.2.6.1 Strain Effect

Two strain effect studies were conducted. In the first study, the mean was varied from 250 to 1750 με at the constant strain amplitude of 250 με. In second study, the maximum strain was increased from 250 to 5000 με with the constant minimum strain of 150 με.

3.2.6.2 Fatigue Effect

Two studies were conducted to evaluate the changes in the dynamic behaviors with respect to fatigue cycle. Table 3-1 presents the variations of the parameters for the fatigue test. The fatigue cycles were applied at two frequencies and amplitudes. In the first study, the fatigue strain was applied sinusoidally between 300 and 3000 με (R=0.1) at 5 Hz or 10 Hz. In the second study, the upper limit of the cyclic fatigue strain was increased to 4000 με and the fatigue cycling was done at only 10 Hz. The upper strain limits were selected to be in the maximum range one might encounter in a dynamically loaded composite structure. Fatigue cycling continued for up to 10^6 cycles. At roughly uniform logarithmic cycles, the dynamic properties were measured with a 1 Hz sinusoid between strains limits of roughly 150 and 1500 με.

Table 3-1: Parameters for the fatigue-damping test.

Material	Fatigue strain (με)	Fatigue frequency (Hz)	Maximum number of cycles
baseline	300-3000	10	10^6
	300-3000	10	10^6
	300-4000	10	10^6
YN10%-TX4	300-3000	5	10^5
	300-3000	10	10^6
	300-4000	10	10^6

3.2.6.3 Temperature Effect

The effect of elevated temperature on the dynamic properties was evaluated. Load cycles were applied at 1 Hz between strains of roughly 150 and 1500 με at temperatures of 21°C, 45°C, and 65°C by using a clear plastic chamber heated by a heat gun which was activated by a digital temperature controller. After gripping the specimen, the chamber is placed around the two grips. The temperature in the chamber is increased based on the feeback signal provided by the tip of a thermocouple which is located near the specimen. Any obvious open slits, holes, and gaps are sealed with insulators and high temperature tape (Figure 3-20, Figure 3-21).

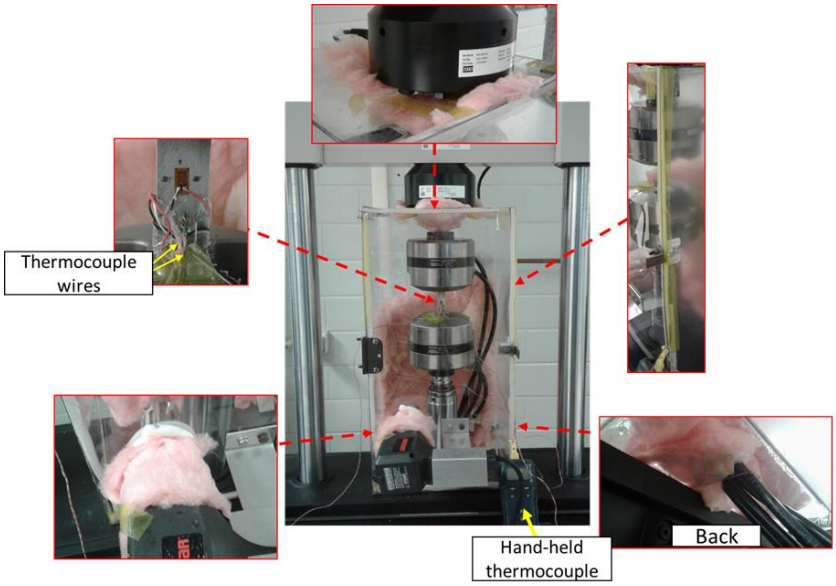

Figure 3-20: Overview of the environmental chamber for the elevated temperature damping test.

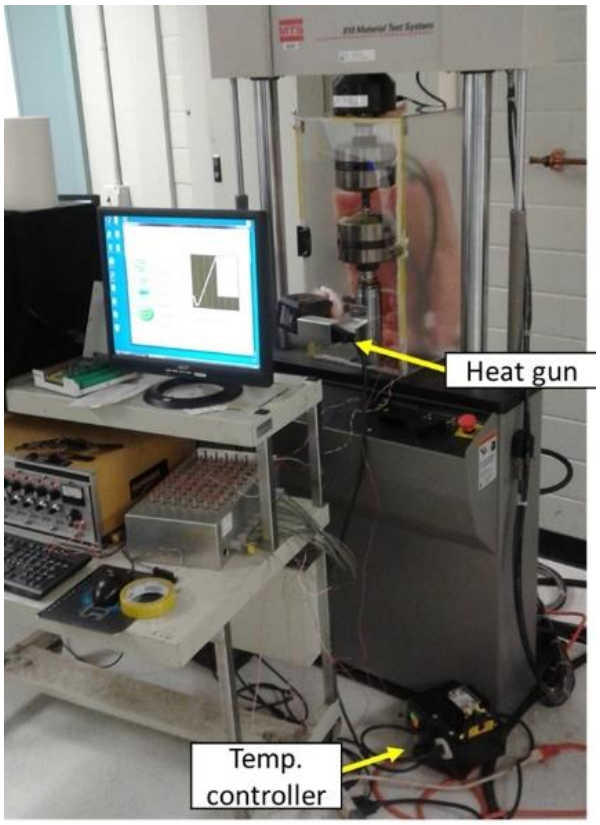

Figure 3-21: Heat gun and temperature controller for the elevated temperature damping measurement.

Before measuring dynamic properties, temperature equilibrated for 15 minutes while the specimen temperature was also checked with an additional hand-held thermocouple. The modulus of elasticity the specimen was measured at each temperature in order to adjust the load range before running damping test. The test setup was also calibrated at each temperature with the aluminum calibration specimen.

3.3 Tensile Strength

Three specimens of the $[0/\pm45]_s$ lamination arrangement, with or without YN10%-TX4, were tested for tensile strength at the rate of 0.5 mm/min on the same MTS load frame as used for

the dynamic tests in order to evaluate how much the addition of yarn affected the strength of c/ep composite laminate.

3.4 Yarn Pullout Test

A pullout test was conducted on the CNT yarn in order to determine the critical shear stress (τ_c), which is one of the vital pieces of information in models predicting the damping from the stick-slip behavior of CNTs (Prakash et al. 2019, Gardea et al. 2015). The pullout test was performed in displacement control on an MTS 810 servo-hydraulic load frame fitted with an MLP-25 110 N (25 lb.) load cell and TMO-2 signal conditioner (both from Transducer Techniques, Temecula, CA). The load cell's output was calibrated with dead weights as shown in Figure 3-22a). Figure 3-22b) is an example of the force unit conversion chart with the conversion equation. The four input signal wires with the gray insulation were connected to TMO-2 signal conditioner, and the output signal wires were connected to the terminal board according to Figure 3-23.

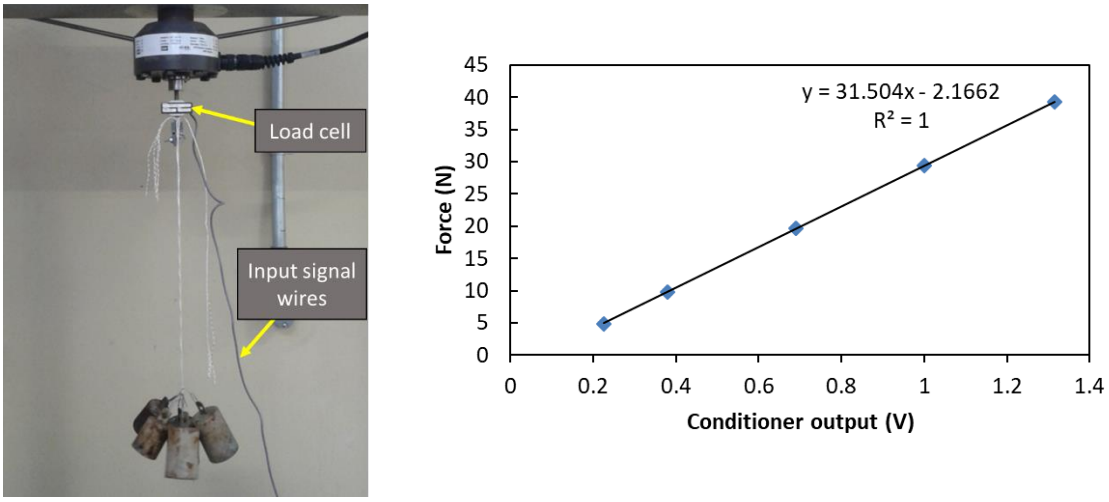

a) b)

Figure 3-22: a) Calibrating and b) converting the output force signal unit for 110 N load cell.

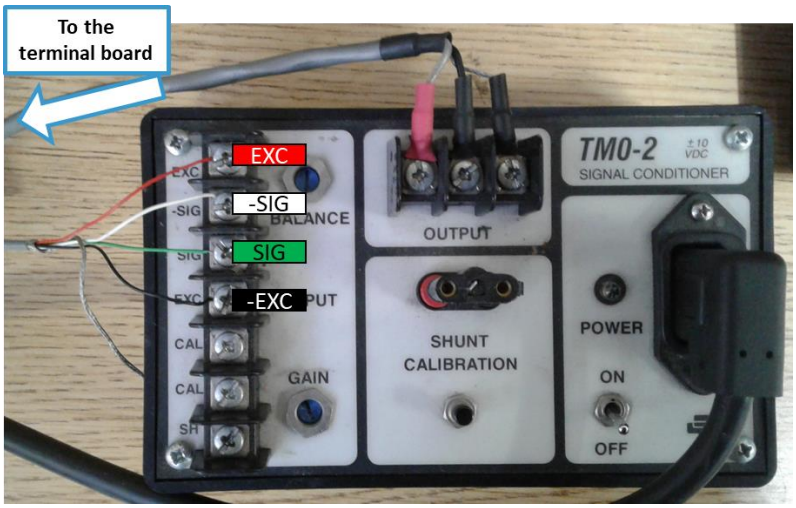

Figure 3-23: Load cell conditioner connection for the pullout test.

Once the calibration step was finished, a small one arm clevis was screwed onto the 110 N load cell and then a threaded screw was passed through the holes. After taping a part of the thread to prevent yarns from being ripped at the root and the crest of the thread when loaded, the CNT yarn of the specimen was tied around the taped area, after which the dangling end of the screw was held with a rope (Figure 3-24).

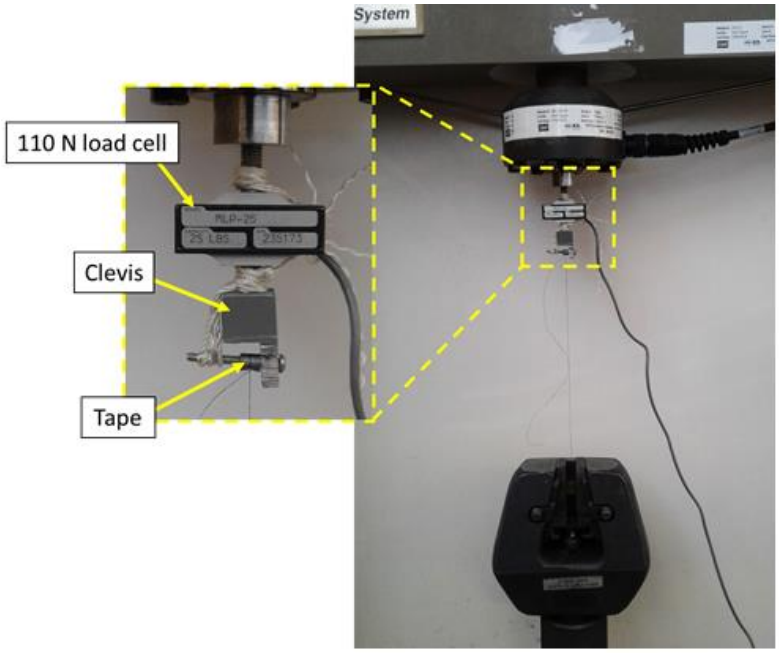

Figure 3-24: Yarn pullout test setup.

The pullout specimen was gripped at the bottom and was pulled at the actuator speed of 0.5 mm/min, while force data was acquired at a rate of 50 Hz. Equation 12 was used to obtain the critical shear stress averaged over the embedment length of the yarn, τ_c,

$$\tau_c = \frac{P_{max}}{\pi d L_e} \tag{12}$$

where

P_{max} = maximum pullout force

d = diameter of yarn

L_e= embedded length

Chapter 4

Results and Discussion

4.1 Specimen Quality Check

4.1.1 Resin Infiltration and Aspect Ratio

Resin infiltration in CNT materials and the constituent volume contents of the baseline material were inspected with SEM in order to check the quality of the specimens. Figure 4-1 shows good resin infiltration into both CNT yarn and long CNT buckypaper. It should be noted that even though Figure 4-1a) is a $[90]_6$ laminate with five interlayers of CNT yarns because the CNT yarns were not distributed evenly and their lengths were not uniform, this particular cross-section showed only one layer of CNT yarns clustered together. Nonetheless, it was observed that only few black regions within the yarn and the buckypaper were noticed, indicating good impregnation of the CNTs and a low overall void content.

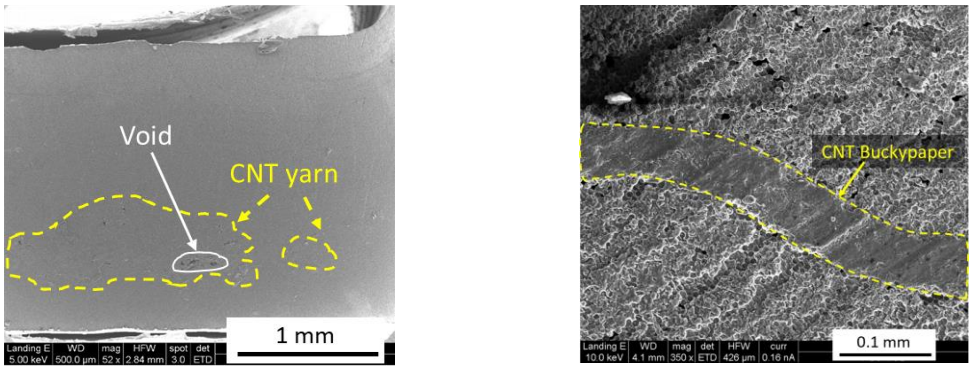

a) b)

Figure 4-1: SEM images of a) CNT yarns in a $[90]_6$ laminate and b) one CNT buckypaper in a $[90]_4$ laminate were taken. Only one interlayer of CNT yarns are shown in Figure 4-1a), and the fibers and the CNT yarns are coming out of the page.

4.1.2 Volume Fraction Analysis

Volume fractions of $[90]_6$ baseline and YN10%-TX4 were analyzed with 30 images at 500× magnification (Table A-4 and Table A-5). However, V_f and V_m of YN10%-TX4 were not measured because the CNT yarns could not be distributed uniformly (Figure 4-1a). Without the uniform distribution of the CNT yarns, V_f and V_m would not be accurate. As seen in Table 4-1, the manufacturing technique induced baseline V_f, V_m, and V_m of 61.1%, 38.4%, and 0.5%, respectively. The low void content is attributed to the beneficial effect of the vacuum applied to the laminate before curing.

Table 4-1: Volume fraction analysis of $[90]_6$ baseline (mean and standard deviation based on 30 images).

Material	V_f(%)	V_m (%)	V_v(%)
$[90]_6$ Baseline	61.1±2.7	38.4±2.6	0.51±0.35
$[90]_6$ YN10%-TX4	N/A	N/A	0.45±0.68

4.2 Damping Test

4.2.1 Repeatability and Limitation

Determining the experimental variation of the test setup as well as the material variation of the baseline materials was the one of the first tasks that had to be tackled in order to differentiate the test variations from an actual change in damping due to the incorporation of the damping materials. Table 4-2 and Figure 4-2 present the material and experimental variations of the dynamic properties for the baseline materials. The columns under the experimental variation header provide statistics based on three separate tests of each specimen. The column under the material variation header provide statistics based on mean values from each of the three

specimens. In general, the tan δ standard deviation of the experimental and the material variation between 0.0003 and 0.0014 regardless of the laminate configuration. As a result, laminates with a low loss factor, such as $[0]_6$, had a high coefficient of variation (CV) (up to 70%), whereas $[90]_6$ and $[45]_6$ laminates had CVs of 10% and 9%, respectively. In the case of the experimental variation study for *E'*, the CV was less than or equal to 1% throughout the ply orientations. Likewise, the material variation study also gave low CV of 1.6% and 1.5% for $[0]_6$ and $[90]_6$, respectively. However, the $[45]_6$ laminate had a high material variation of 13.2% because obtaining shear damping properties required stress and strain transformation from the use of 45° triaxial rectangular rosette, all of which introduced more human errors such as properly aligning strain gages on the right stress state. It was concluded from this investigation the highest CV of tan δ was 70%, 10%, and 9% for $[0]_6$, $[90]_6$, and $[45]_6$ laminates, respectively. The highest CV of *E'* and *G'* was found to be 1.6% and 13.2%, respectively.

Table 4-2: Material and experimental variations of $[0]_6$, $[90]_6$, and $[45]_6$ baseline laminates. Results given as mean ± standard deviation and CV in parentheses.

Laminate	Material Property	Experimental Variation			Material Variation
		Specimen 1	Specimen 2	Specimen 3	
$[0]_6$	tan δ	0.0026 ± 0.0007 (26.9%)	0.0021 ± 0.0011 (52.4%)	0.0020 ± 0.0014 (70%)	0.0022 ± 0.0003 (13.6%)
	E' (GPa)	131 ± 1.1 (0.8%)	133 ± 1.3 (1.0%)	129 ± 1.1 (0.9%)	131 ± 2.1 (1.6%)
	E'' (MPa)	343 ± 89 (25.9%)	273 ± 146 (53.5%)	260 ± 184 (70.8%)	292 ± 45 (15.4%)
$[90]_6$	tan δ	0.0091 ± 0.0003 (3.3%)	0.0077 ± 0.0004 (5.2%)	0.0078 ± 0.0008 (10.3%)	0.0082 ± 0.0008 (9.8%)
	E' (GPa)	8.6 ± 0.074 (0.9%)	8.6 ± 0.017 (0.2%)	8.4 ± 0.011 (0.1%)	8.5 ± 0.13 (1.5%)
	E'' (MPa)	78 ± 2.4 (3.1%)	66 ± 2.9 (4.4%)	66 ± 6.5 (0.8%)	70 ± 7 (10%)
$[45]_6$	tan δ	0.012 ± 0.0006 (5%)	0.014 ± 0.0004 (2.9%)	0.011 ± 0.0004 (3.6%)	0.012 ± 0.0011 (9.2%)
	G' (GPa)	4.4 ± 0.0032 (0.1%)	5.7 ± 0.019 (0.3%)	4.9 ± 0.056 (1.1%)	5 ± 0.66 (13.2%)
	G'' (MPa)	55 ± 2.4 (4.4%)	78 ± 2.0 (2.6%)	56 ± 1.8 (3.2%)	63 ± 13 (20.6%)

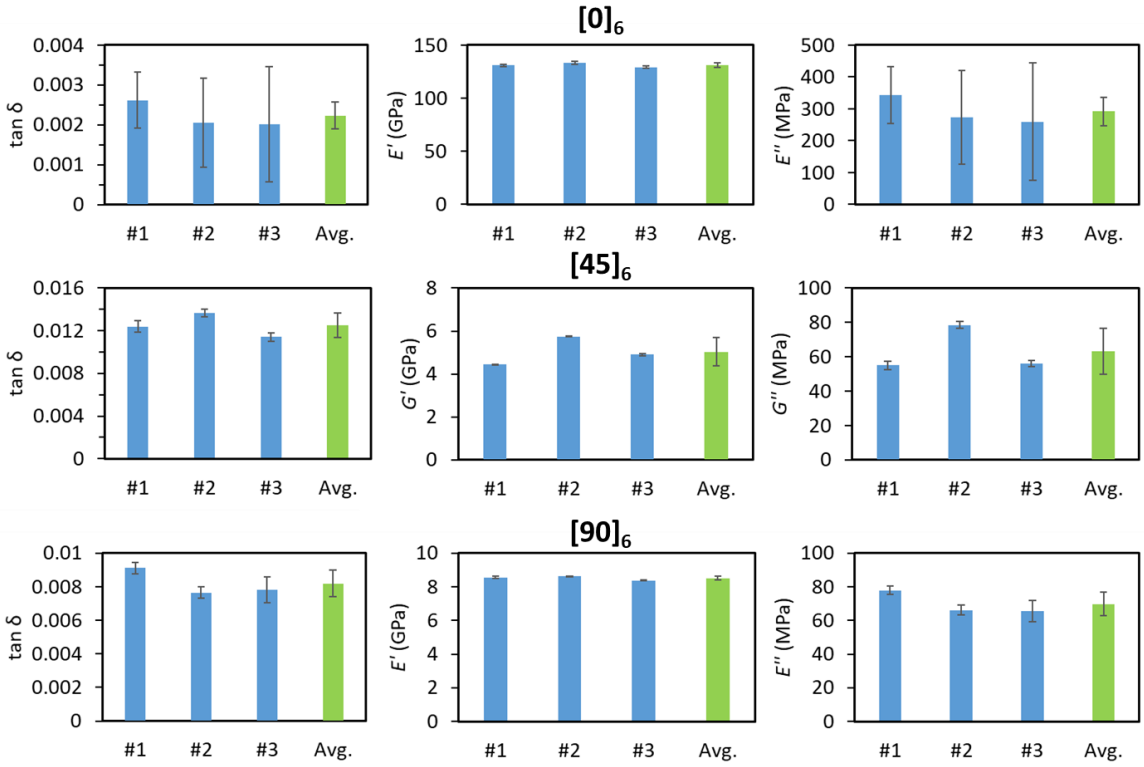

Figure 4-2: Material and experimental variations for $[0]_6$, $[90]_6$, and $[45]_6$ baseline laminates. Bars show averages and standard deviations.

Damping tests were conducted on the aluminum calibration specimen at various load amplitudes in order to determine the minimum range at which the test setup could collect consistent raw phase difference (Figure 4-3). The result showed that the raw phase difference was inconsistent until 76 N and became consistent after 98 N at which the strain amplitude was 93 με, based on the raw phase difference being close to the mean and standard deviation of 9 repeated test performed at a 236 N load amplitude. This result was used to establish that composite laminates need to be designed for a minimum load amplitude of 96 N and strain amplitude of 93 με in order to obtain consistent phase difference data.

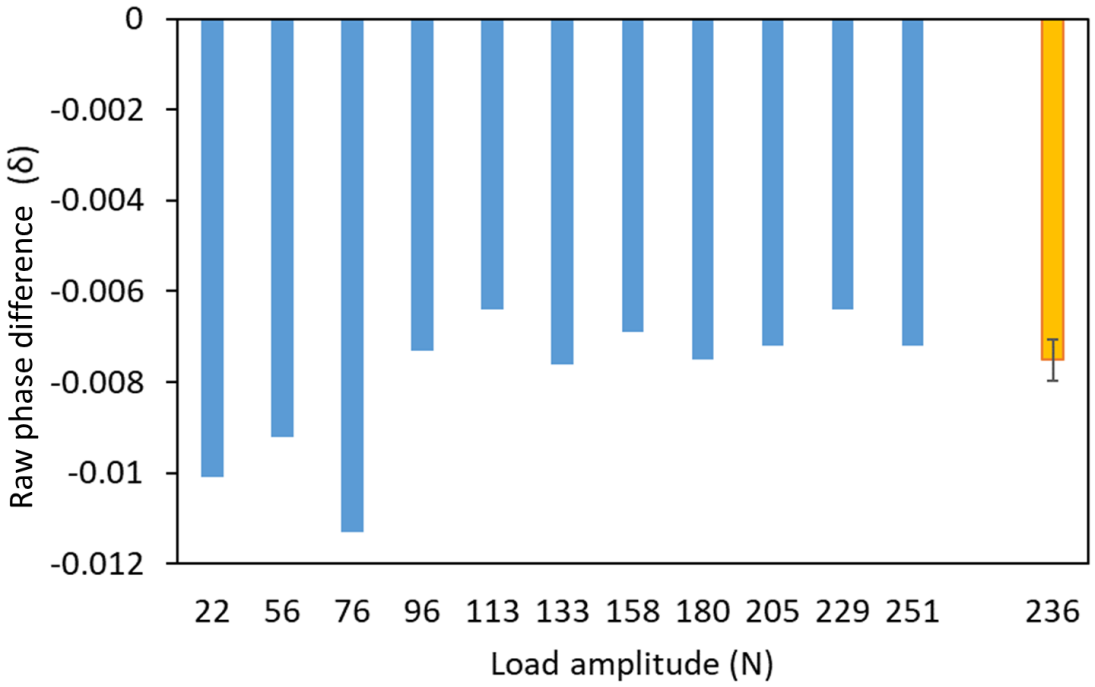

Figure 4-3: Showing raw phase difference at different load amplitudes for the aluminum specimen. The 236 N bar shows the average and standard deviation from 9 repeated tests.

4.2.2 Material Selection

With the knowledge of test variations, various materials with the potential of damping increase were investigated on the matrix dominant $[90]_6$ baseline laminate that could show more change in damping than on the fiber dominant $[0]_6$ laminate (Figure 4-4). The result of the preliminary exploration for damping materials showed that VDP, GBP, and YN noticeably increased loss modulus. VDP in particular seemed to be promising because the loss factor was increased by nearly 900%. However, the storage modulus decreased by 70%. The overall dissipation of energy represented by the loss modulus was still greater in VDP than the baseline even with the 70% drop of storage modulus. Even so the reduction of modulus to this degree could not be suitable for blade applications, not to mention the inherent temperature sensitivity of VDP towards the damping behavior. Unlike VDP, GBP and YN increased both the loss factor

and storage modulus. It was shown that GBP gave more contributions to the baseline than YN, but the two materials could not be compared directly to each other due to the different amount of CNTs in each. Both of these materials were considered as good candidates for further evaluation until it was realized during the resin infiltration study that GBP could not be fully impregnated with resin due to its high density, as demonstrated in Figure 4-5 where the GBP was easily delaminated. Since YN showed good resin impregnation unlike GBP, CNTs were chosen for further evaluation.

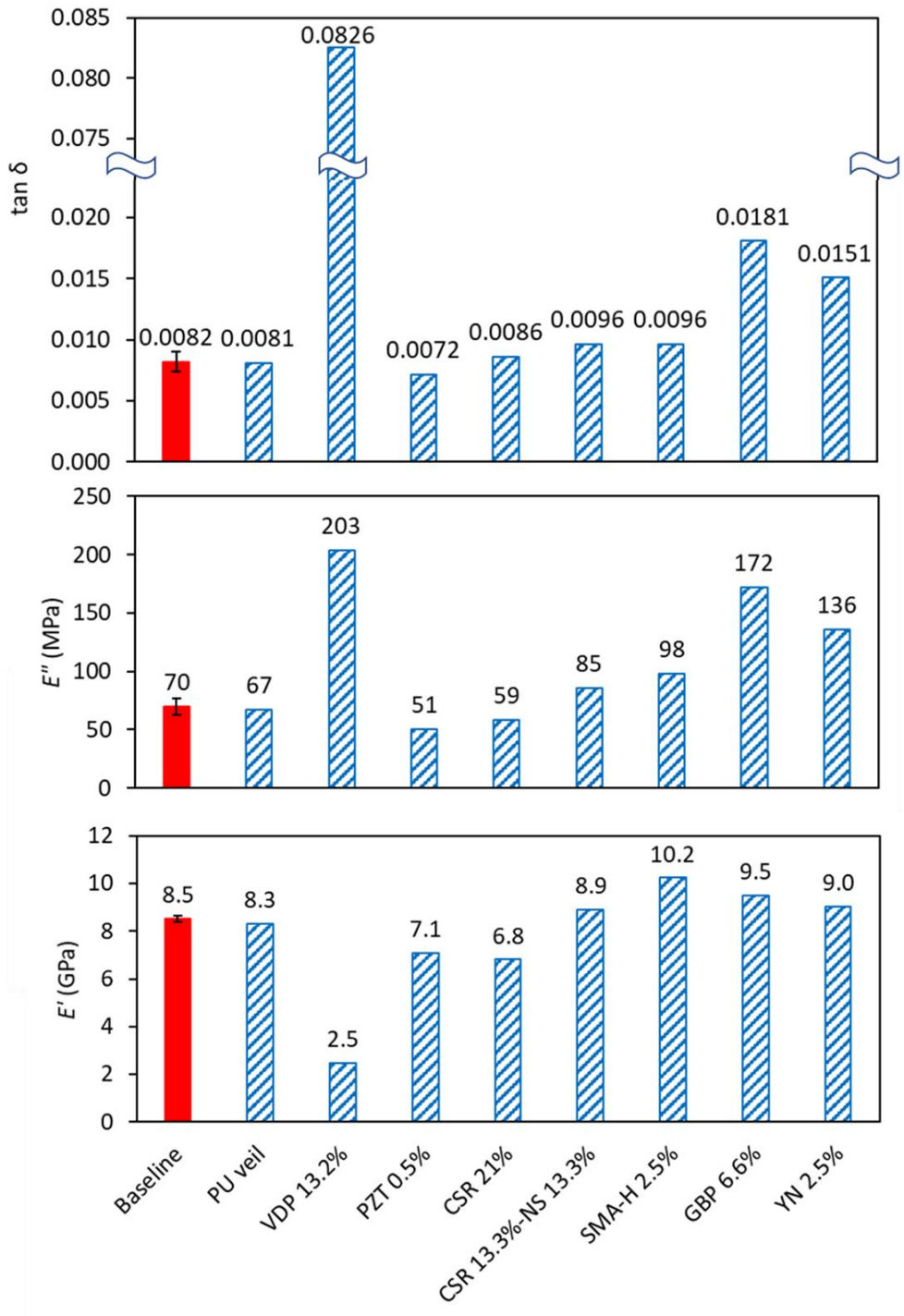

Figure 4-4: Dynamic properties of $[90]_6$ laminates with the exploratory damping materials. For the baseline only, the mean and standard deviation based on three different specimens tested three times each, as detailed in Table 4-2, is shown. Other materials were tested once.

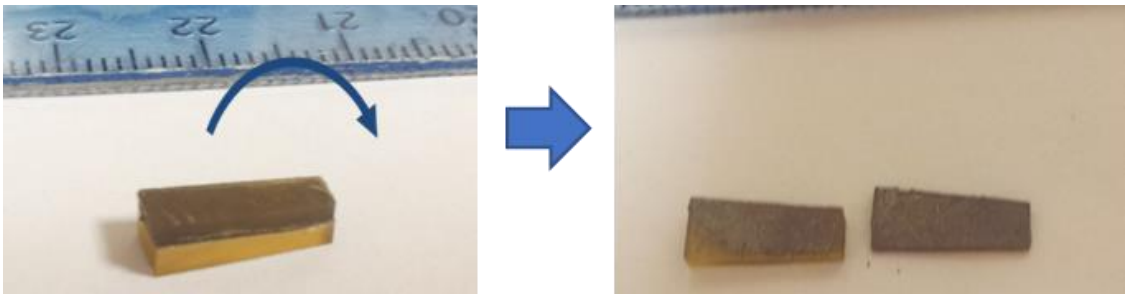

Figure 4-5: Splitting GBP in resin.

As CNT was selected as the material of interest from the preliminary experiments, different types of CNTs and surfactants were investigated next. Figure 4-6 shows the dynamic properties for various combinations of CNTs and surfactants. 1.3 vol.% of CNT and 1:0.76 ratio of surfactant was added in each combination to identify promising materials for increasing the damping properties. According to the result, three combinations with buckypapers had negligible change or even reduction of damping. Unlike either of the buckypapers, CNT yarn not only increased the loss factor and loss modulus but also increased the storage modulus. This result was possible because CNTs are aligned in CNT yarns whereas they are randomly oriented in buckypaper. The effect of alignment of CNT yarns will be further addressed in the following section. Between the two surfactants, Triton X-100 induced superior result over SDS with 39% and 6.4% increase in loss factor and loss modulus compared to the baseline, respectively. The smaller amount of Triton X-100 than SDS to reach CMC was the likely cause that Triton X-100 needed less amount to affect the interfacial bond strength.

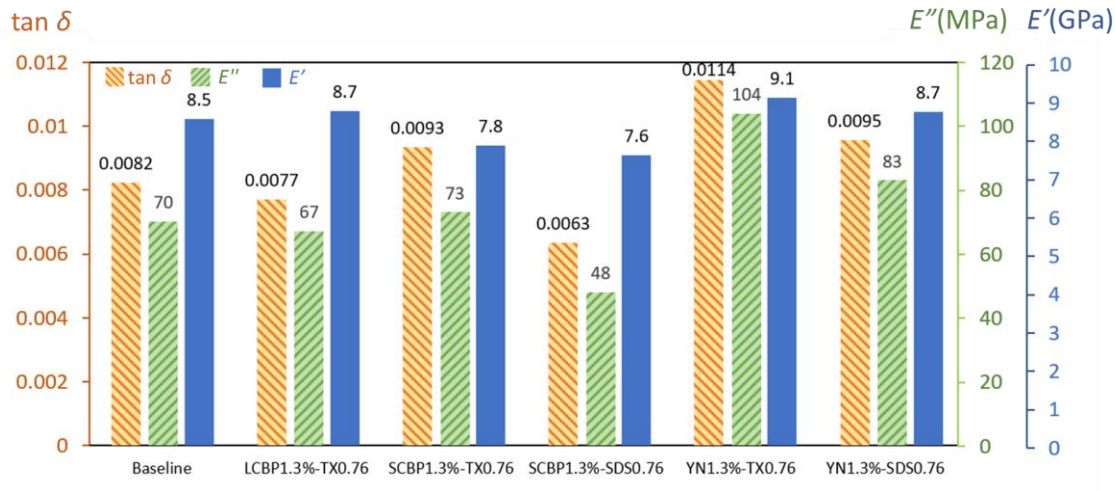

Figure 4-6: Dynamic properties of $[90]_6$ laminate with different combinations of CNT and surfactant tested at strains between 1000 με and 1500 με. Except for the baseline, each material combination was test once.

4.2.3 Material Design - CNT and Surfactant Concentration

Devalve and Pitchumani 2013 increased damping by 133% by dispersing 2 wt.% of CNT in carbon/epoxy composite. In this study, selected choice of materials, the CNT yarn and Triton X-100, presented in the previous section were used to increase the volume fraction of CNT and adjust the amount of surfactants under the assumption that the surfactants affect the bond strength between CNTs and epoxy. the interfacial strength.

As shown in Table 4-3, damping of $[90]_6$ laminate increased monotonically with the volume percent of CNT yarn. 10% CNT yarn resulted in 388% increase in damping when it was tested at strain amplitude of 250 με. The improvement was possible because not only the yarn form made it feasible to add high concentration of CNTs but the CNTs themselves were also aligned in the loading direction which induced more slippage than in the random direction (Liu et al. 2006). Figure 4-8 compares the tan δ increase from adding YN in the loading direction and the

fiber direction, which represents the random orientation. As it can be seen, the damping improvement from the CNTs was more effective when they were aligned in the loading direction. At the same time, the alignment was also the very reason stiffness increased, which is observed from the result where the storage modulus of $[90]_6$ YN 10% increased by 29%. The fact that placing CNTs in the loading direction was better than placing them in the fiber directions of the $[0/\pm45]_s$ laminate suggested that the axial damping properties had more influence than the shear damping properties on increasing damping through stick-slip mechanism.

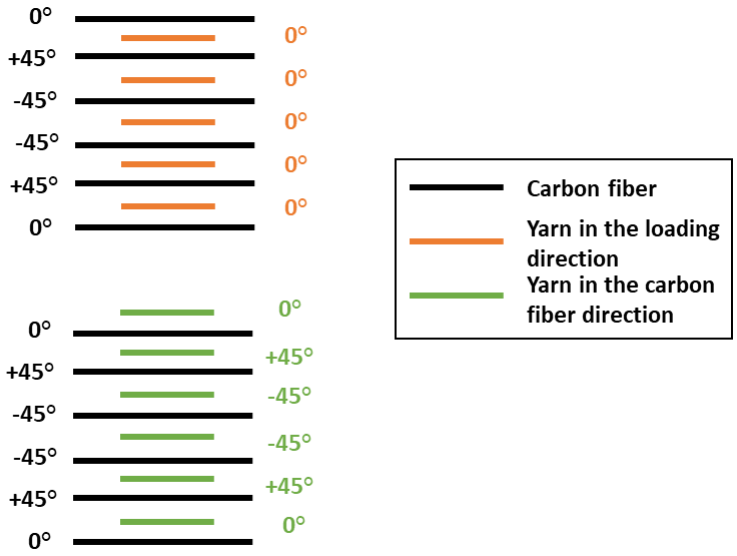

Figure 4-7:Diagram of different CNT yarn layups in $[0/\pm45]_s$ laminate.

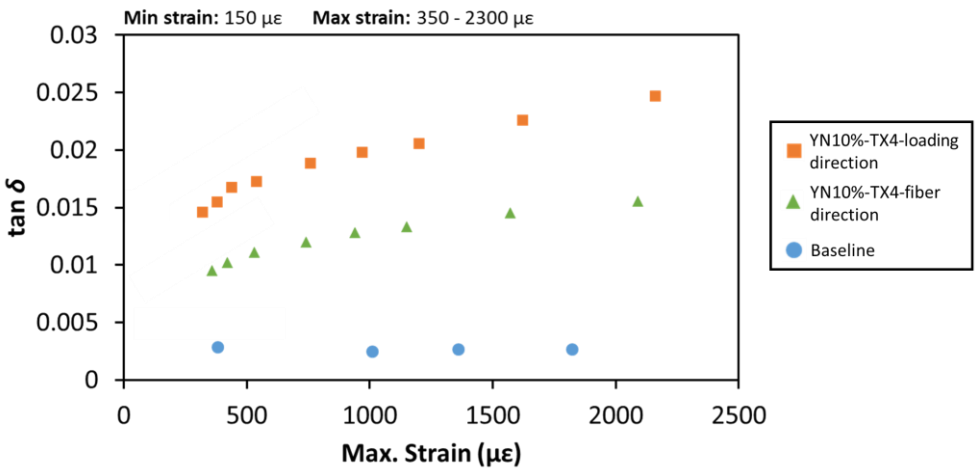

Figure 4-8: Comparison of CNT yarn oriented in the loading and fiber direction for $[0/\pm45]_s$ laminate. The stacking sequences of the YN10%-TX4 laminates are described in Figure 4-7.

Table 4-3: Evaluating the concentrations of TX and YN in the loading direction on $[90]_6$ laminates tested at strains between 1000 με and 1500 με.

Material system	CNT volume percent	CNT:Surfactant	tan δ	E' (GPa)	E'' (MPa)
Baseline†	--	--	0.0082 ± 0.0008	8.5 ± 0.13	70 ± 7.0
YN 2.5%	2.5%	--	0.0151	9.0	136
YN 10%	10%	--	0.0400	11.0	439
TX 1:2	--	1:2	0.0222	7.1	158
TX 1:4	--	1:4	0.0502	5.6	279
YN 10%-TX 1:2	10%	1:2	0.0447	13.4	598
YN 10%-TX 1:4	10%	1:4	0.0485	13.6	659

† The mean and standard deviation based on three different specimens tested three times each, as detailed in Table 4-2

Triton X-100 also caused monotonic increase in both the loss factor and loss modulus. Triton X-100 decreased the storage modulus due to resulting in low interfacial shear strength. However, the effect of Triton X-100 and CNT yarn balanced the gain and the loss of stiffness, producing synergistic effect of high stiffness and damping. The combination of CNT yarn 10% and TX 1:4 increased tan δ, E', and E'' by 491%, 60%, and 841%, respectively. As the preliminary study showed tan δ increase of 491% even at low strain amplitude of 250 με, the

result indicated that the incorporation of high concentration of CNTs in composite materials for high damping was feasible.

4.2.4 Damping Conditions

In this section, the effects of strain, fatigue, and temperature were investigated using the $[0/\pm45]_s$ YN10%-TX4 laminates.

4.2.4.1 Strain Effect

The strain amplitude study agreed with the previous experimental study conducted on nanocomposites without continuous fibers and behaved in a non-linear fashion even for stiff c/ep composite as suggested by the models from the literature (Prakash et al. 2019, Gardea et al. 2015). The complex modulus approach was used even in circumstances where the stick-slip behavior introduced non-linear damping with respect to strain. As the complex modulus method did not capture non-linearity, dynamic properties were measured at different strain level in order to observe the non-linear trend. As seen in Figure 4-9 and Figure 4-10, the slope of the YN10%-TX4 loss factor increased rapidly with the strain amplitude from 350 to 550 με, after which the slope began to decrease but still maintained the linear slope. The individual data points can be found in Table A-6.

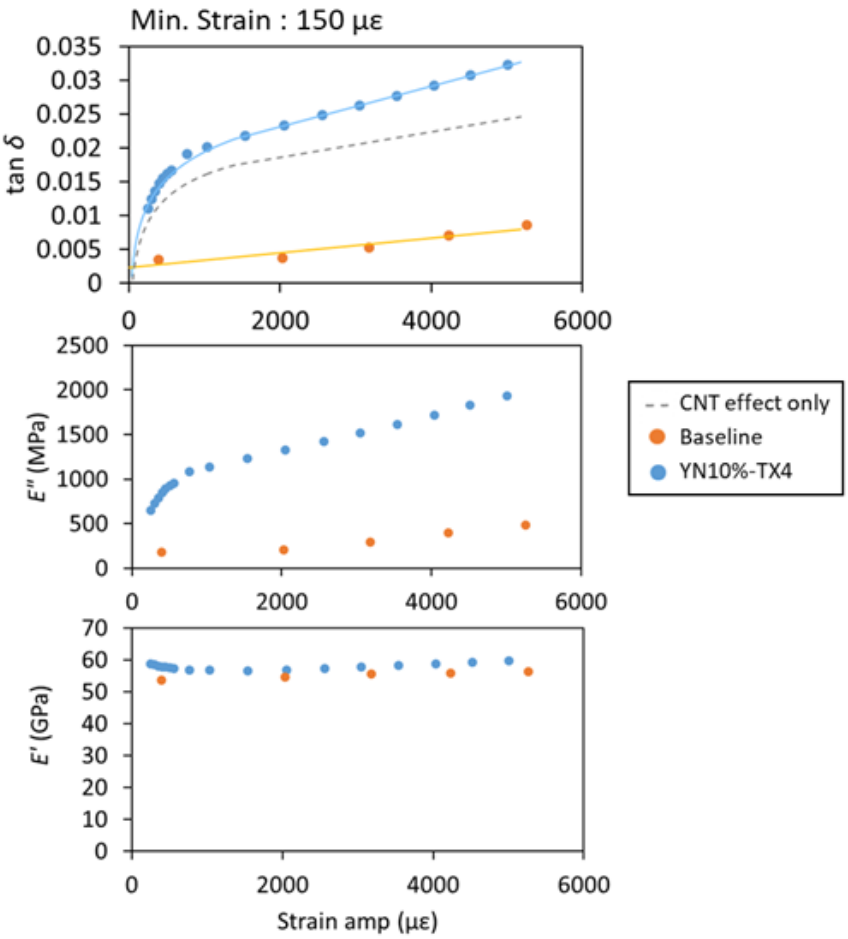

Figure 4-9: The effect of strain amplitude on the dynamic properties of $[0/\pm45]_s$ baseline and 10%YN-TX4 laminates.

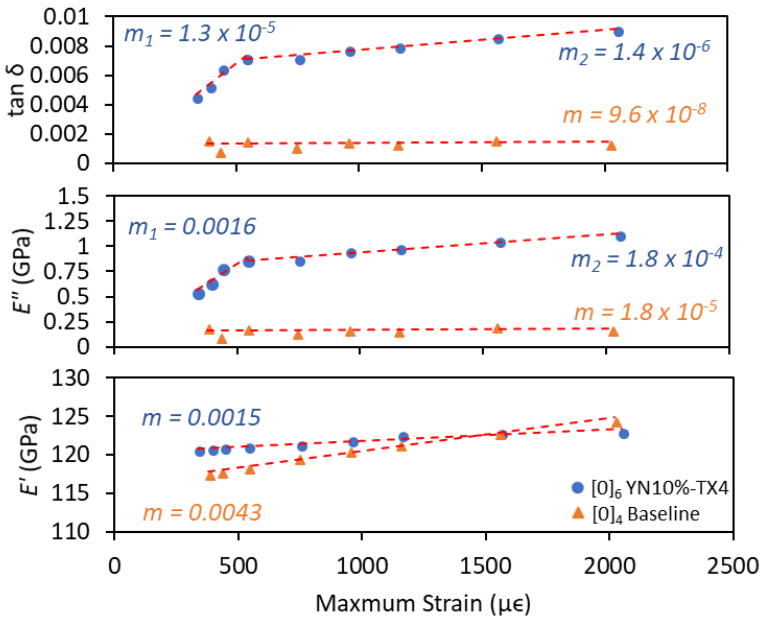

Figure 4-10: The effect of maximum strain on the dynamic properties of $[0]_6$ baseline and $[0]_4$ YN10%-TX4 laminates.

In both of the laminates, unlike YN10%-TX4, the baseline had consistent linear rate from the beginning. As seen in Table 4-4, the tan δ line was fitted with the logarithmic equation from 0 to 1430 με and the linear equation afterwards. Two straight lines were fitted in the case of the $[0]_6$ laminate, as opposed to the logarithmic and straight line in the case of the $[0/\pm45]_s$ laminates.

Table 4-4: Equations of the fitted lines for the strain amplitude study performed on the $[0/\pm45]_s$ laminates

Fitted line	**Equation**[†]	
Baseline	$y = (1.1087\text{E}{-6})x + 0.00226$	
YN10%-TX4	$y = 0.0057\ln(x) + 0.02$	$0 < x < 1430$
	$y = (3\text{E}{-6})x + 0.0171$	$x > 1430$

[†] x = microstrain, y = tan δ

Due to the presence of linear damping increase with respect to increasing maximum strain even in the baseline material, the difference of the baseline and the damping material was taken in order to observe only the damping effect of CNTs, which is represented by the gray dashed line. This

difference still showed steep increase initially but then started to plateau afterwards, supporting the idea of stick-slip theory that CNTs dissipate more energy through friction and the van der Waals forces created when CNTs slip and slide continuously during the cyclic load. One limitation of the study was that the onset of stick-slip could not be observed due to the low signal to noise ratio of the test setup at lower strain amplitude than 350 με. Nonetheless the strain amplitude study supported the idea that the stick-slip effect not only increased the damping properties without affecting storage modulus but also presented strain dependent behavior of damping which strengthened the stick-slip theory. Although the damping behavior could not be observed at the onset site, the damping materials nonetheless induced 310% and 340% increase in tan δ and E'', respectively, while only 10% increase in E'. In the same study conducted in $[0]_6$, the damping materials increased tan δ and E'' by 560% and decreased E' by 1% (Figure 4-10). In order to determine significance of the damping enhancement of the two laminates, the data points were plotted on the stiffness-damping plot shown in Figure 4-11. As it is shown, although the diagonal line in the graph was the line that the typical materials could not cross, both laminates with YN10%-TX4 were able to cross the line and ultimately raising the limit (Dong and Lakes 2013).

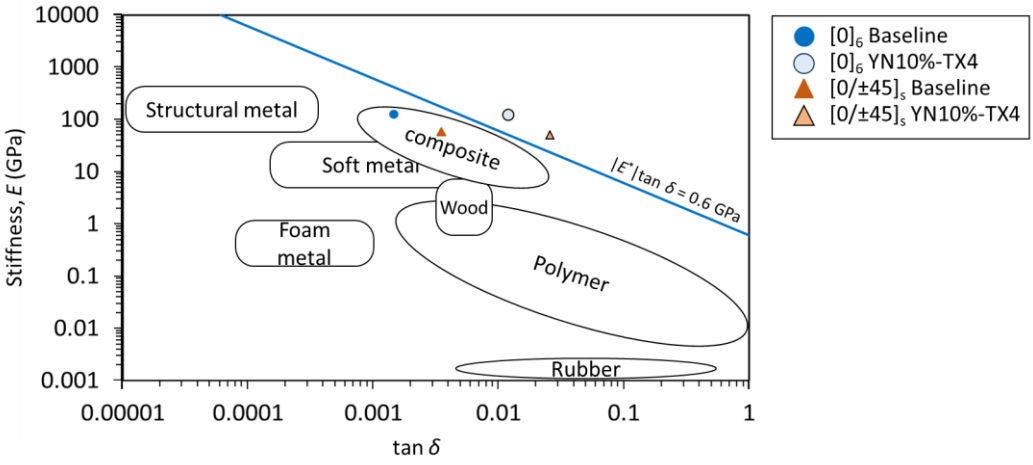

Figure 4-11: Comparison of baseline and YN10%-TX4 in $[0]_6$ and $[0/\pm45]_s$ laminates on stiffness-damping plot.

Meanwhile the mean strain study did not present any dramatic changes to the dynamic properties as did the strain amplitude study but nevertheless provided relevant information that led to further insight into the stick-slip theory. Figure 4-12 shows the dynamic properties as a function of mean strain with the constant strain amplitude of 250 με (Table A-7).

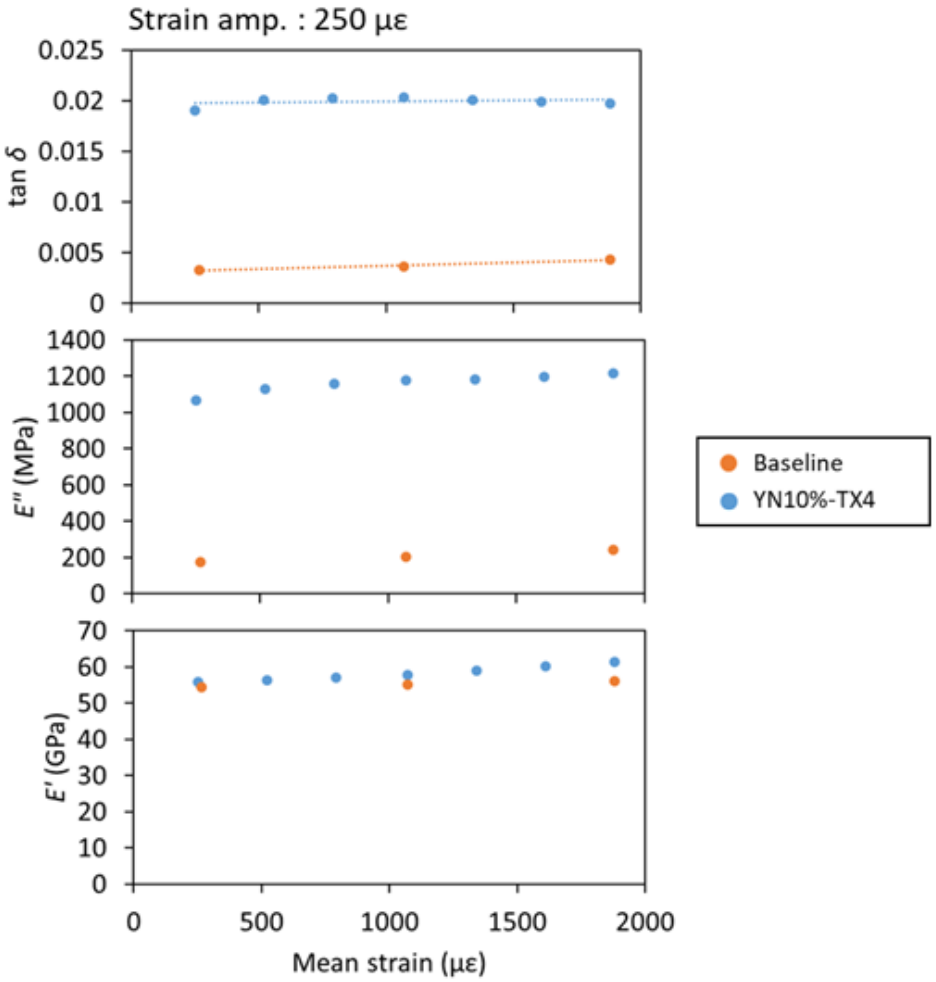

Figure 4-12: The effect of mean strain with constant strain amplitude of 250 με on dynamic properties for $[0/\pm45]_s$.

As shown in Figure 4-12 above, the properties remained unchanged throughout the mean strain in both the $[0/\pm45]_s$ baseline and YN10%-TX4 laminates, although, the addition of the yarns gave constant damping increase of 450% as well. The presence of constant values gave useful information that CNTs provide consistent damping as long as the cyclic strain does not change regardless of how much they are pre-strained. The constant value was an indication that the cyclic amplitude was enough to completely slip the CNTs, otherwise, the partial slippage of the CNTs would lead to different amount of damping increase at different mean strain. In the situation where static load is applied, for example, due to the centrifugal force on blades during rotation, the amount of damping that is applied could be easily predicted by knowing the amplitude of the cycle load or vibration.

4.2.4.2 Fatigue Effect

The dynamic properties of $[0/\pm45]_s$ baseline and YN10%-TX4 were evaluated with respect to fatigue loading cycles in order observe the consistency of the YN10%-TX4 damping behavior. Figure 4-13 presents the result of fatigue-damping studies conducted up to 10^6 fatigue cycles at 10 Hz under two strain levels, 300-3000 με and 300-4000 με. The damping test was performed twice after each fatigue cycle at 1 Hz and at 150-1500 με. What must be noted is that the *E'* values of the two baseline materials were different by 5 GPa as a result of cutting specimens from different c/ep plates. The individual data points can be found in Table A-8~Table A-12.

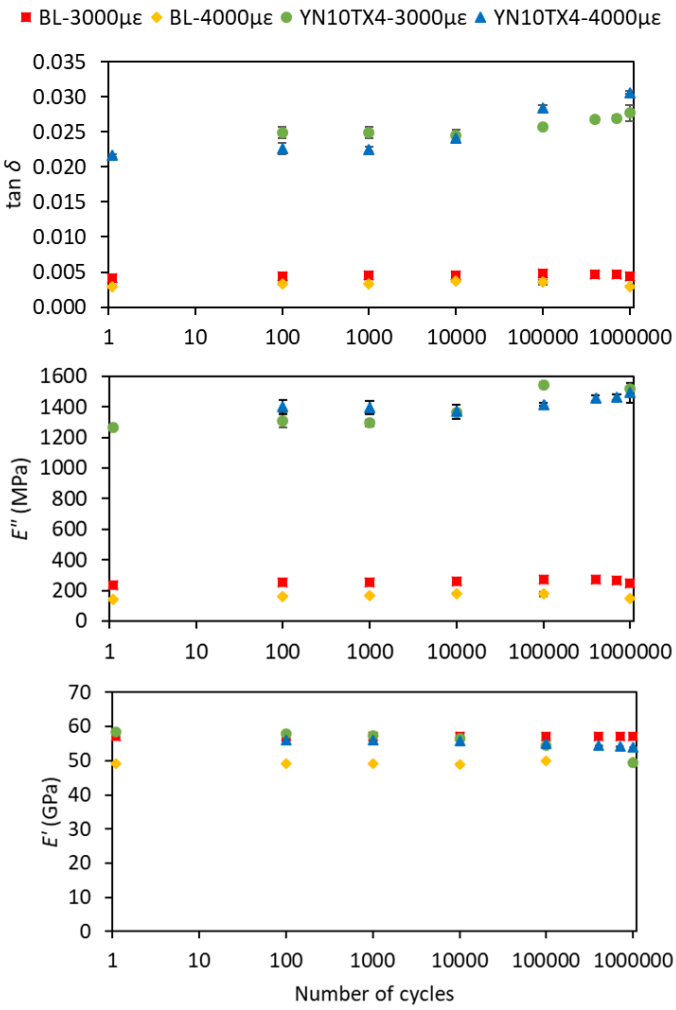

Figure 4-13: The effect of fatigue cycles on dynamic properties for $[0/\pm45]_s$. Each point is an average of two repetitions and has a scatter bar representing the maximum and the minimum measurements.

In general, the dynamic properties of the baseline remained constant at either of the strain levels throughout the number of fatigue cycles. However, the YN10%-TX4 had more interesting behavior. Similar to the baseline, YN10%-TX4 tested at 300-3000 με maintained steady state of the dynamic properties for the most part up until 10^6 cycles when tan δ was increased by 11% and *E'* was decreased by 4%. However, increasing the strain level to 300-4000 με range where even the strain gages failed after 10^5 cycles was what affected YN%-TX4 the most. At this strain level,

strain gages on both the front and back were replaced after 10^5 cycles, as well as after 10^6 cycles. As shown by the green circular data points in Figure 4-13, tan δ and E' had noticeable change. After 10^6 cycles, tan δ was increased by 42% whereas E' dropped 15%, which was a clear indication that the microcracks due to fatigue was forming and therefore lead to further damping increase.

In addition to the fatigue study at two strain levels, fatigue tests were performed at 5 Hz and 10 Hz to determine if fatigue cycling rate had any effect on the variation of damping properties with fatigue cycles. The damping test was performed twice after each fatigue cycle at 1 Hz and at 150-1500 με. However, the damping test was performed only once after 10^3 fatigue cycles. As shown by the Figure 4-14, the two frequencies of the fatigue test showed about the same results of the properties for YN10%-TX4 up to 10^5 cycles. It was concluded from the study that fatigue cycling could be conducted at either frequency and the dynamic test results would not change.

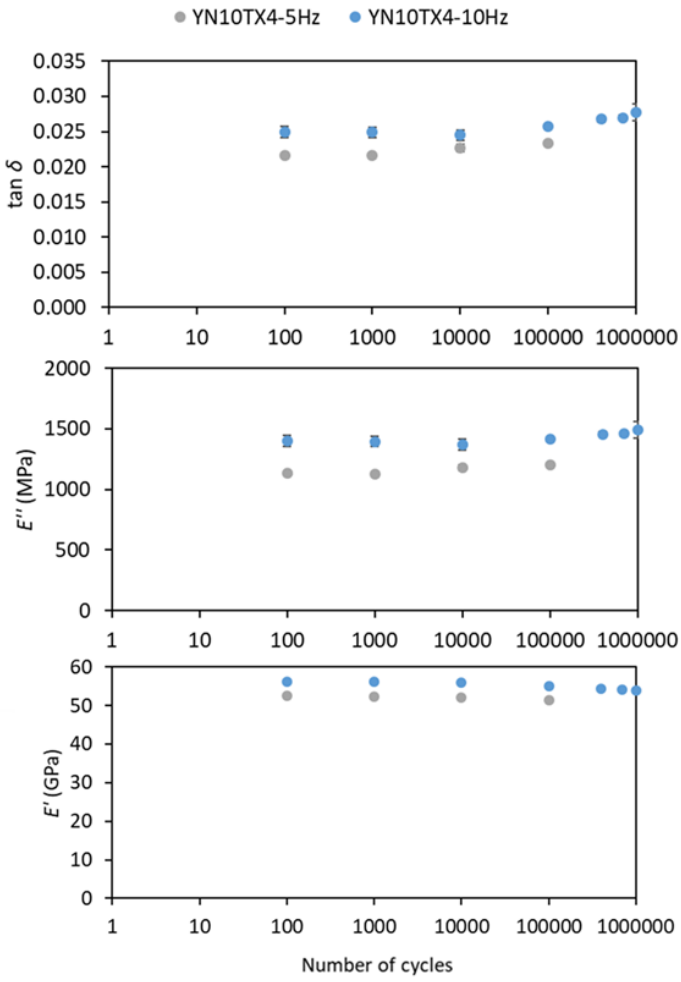

Figure 4-14: Comparing the dynamic properties of $[0/\pm45]_s$ tested at fatigue frequencies of 5 Hz and 10 Hz.

4.2.4.3 Temperature Effect

Temperature controlled test was conducted in order to investigate the temperature effect on the dynamic properties of $[0/\pm45]_s$ baseline and YN10%-TX4 laminates. As seen in Figure 4-15, tan δ and *E"* gradually increased at elevated temperature, whereas the *E'* decreased in value. The individual results are shown in Table A-13. The results were an expected outcome for polymeric materials since the brittle state at room temperature changes to rubbery state at an

elevated temperature as it gets closer to the glass transition temperature (T_g) (Rudin and Choi, 2012). As an example, T_g of the 862W resin cured according to the curing schedule mentioned in Section 4.2 is 150°C (Vashisth et al. 2018).

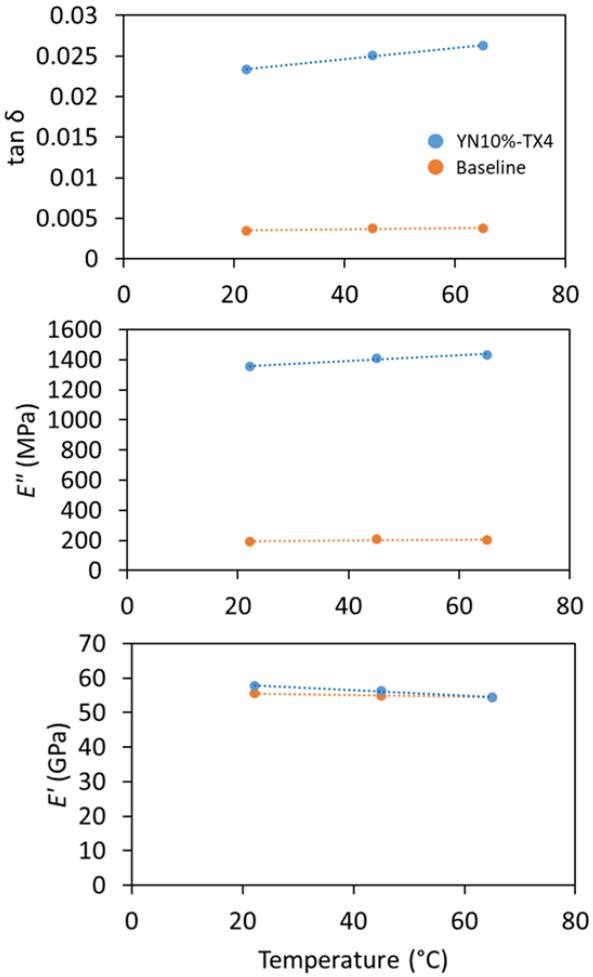

Figure 4-15**:** Effect of elevated temperature on the dynamic properties of $[0/\pm45]_s$ baseline and YN10%-TX4 laminates.

4.3 Tensile Strength

Tensile strength was checked in order to evaluate any changes in the strength by adding CNT yarns to the composite. As it is shown in Figure 4-16, the addition of yarns and Triton X-100 did not reduce the tensile strength of the $[0/\pm45]_s$ laminate. Although the negligible effect of CNT yarn on the strength of c/ep laminate was shown, further investigation should be made on the matrix dominated specimens because it was evident from the fatigue-damping relationship study that the $[0/\pm45]_s$ YN10%-TX4 laminate showed signs of subcritical damage that was likely to be the matrix damage. Individual data points can be found in Table A-14.

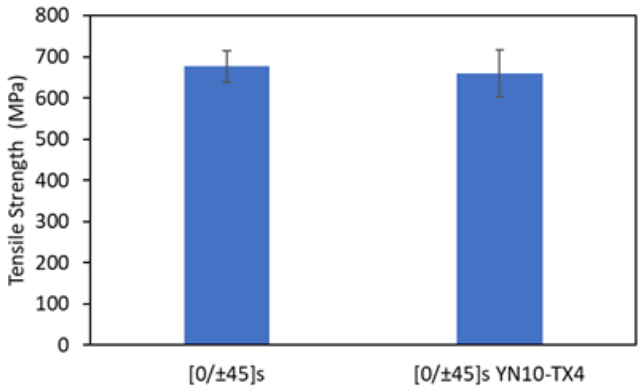

Figure 4-16: Tensile strength of $[0/\pm45]_s$ with and without YN10%-TX4.

4.4 Yarn Pullout Test

The yarn pullout test gave a vital piece of information for modelling the stick-slip behavior of CNT yarns with the diameter of 0.015 cm. Figure 4-17 presents the critical shear strength, τ_c, and its maximum pullout force, P_{max}, required as a function of embedded length. As suggested by the Equation 11 in which the τ_c was assumed to be constant along the embedment length, the force continued to increase linearly with embedment length. Regardless of the change in the embedded length and its corresponding maximum force to pull out the CNT yarn, τ_c

remained constant at the average of 2.01 ± 0.4 MPa. The individual data points of the maximum force and τ_c are shown in Table 4-5.

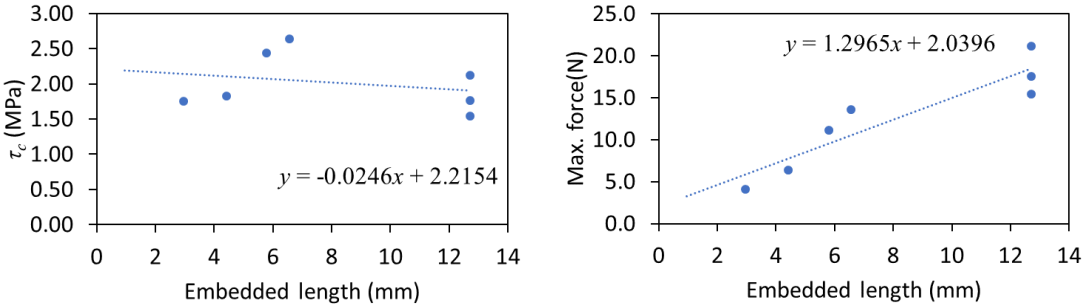

Figure 4-17: Maximum force and τ_c as a function of embedded length.

Table 4-5: Individual data points of maximum force and τ_c for the yarn pullout test.

Epoxy Material	Specimen #	Embedment length (mm)	Max. force (N)	τ_c (MPa)
862W:TX100 (1:1)	1	6.6	13.6	2.6
	2	5.8	11.1	2.4
	3	2.9	4.0	1.8
	4	4.4	6.4	1.8
	5	12.7	15.4	1.5
	6	12.7	21.2	2.1
	7	12.7	17.6	1.8
	Average		12.7	2.0
	Sdev.		6.1	0.40

Chapter 5

Conclusions and Recommendations

5.1 Conclusions

High stiffness-damping augmentation of CNTs in c/ep composite was evaluated in this experimental investigation. In order to obtain damping with the uniform strain field through the thickness in the gage section of specimens, a damping test facility and procedure were developed using a servo-hydraulic MTS machine operated in the tension-tension mode. The sinusoidal damping frequency, the minimum strain, and the maximum strain were set at 1 Hz, 1000 με, and 1500 με, respectively, as the primary conditions for comparing and evaluating the dynamic properties. Among the three strain measurement techniques, which were strain gage, extensometer with silicone adhesive, and extensometer with cyanoacrylate adhesive, the strain gage induced the lowest standard deviation of the phase difference. The standard deviation of tan δ for all of the unidirectional baseline laminates was between 0.0003 and 0.0011. The material variation of E' and G' were found to be 1.6% and 13.2%. Obtaining shear storage modulus led to more to human error due to the usage of a 45° triaxial rectangular rosette.

Among the candidate damping materials inserted in the $[90]_e$ laminate, the combination of CNT yarn and Triton X-100 led to the most damping enhancement without reducing stiffness of c/ep laminate. High CNT volume fraction of up to 10% in c/ep composite laminates was achievable with CNT yarn for the purpose of increasing damping. The tensile strength of $[0/\pm45]_s$ baseline and YN10%-TX4 were 677±38 MPa and 660±57 MPa, respectively.

The strain amplitude and mean strain effects of YN10%-TX4 were investigated to evaluate the strain dependent behavior. As the stick-slip theory suggested strain-dependent behavior of damping, while the minimum strain was at 150 με the addition of YN10%-TX4 resulted in steep damping increase until the maximum strain of 550 με, after which the slope began to decrease. At 5000 με, tan δ, E'', and E' were increased by 310%, 340%, and 10%, respectively, in $[0/\pm45]_s$ layup with the addition of YN10%-TX4. On the other hand, the variation of mean strain from 250 με to 1880 με with a constant strain amplitude of 250 με did not affect the dynamic properties, indicating that the CNTs completely slipped at this strain amplitude. In addition, the pullout test was performed on the CNT yarns with the same amount of Triton X-100 in resin as in YN10%-TX4, and the critical shear strength was measured to be 2.01 MPa.

The damping performance with respect to temperature and fatigue was also investigated. Under the condition of the elevated temperature up to 65°C, the temperature moderately increased tan δ and E'' but decreased E' of baseline and YN10%-TX4 to a similar degree. In the fatigue study, the dynamic properties of YN10%-TX4 were consistent even at 10^6 cycles under 300-3000 με. However, increasing the fatigue strain to 300-4000 με led to decrease in E' and increase in tan δ beyond 10^5 cycles. At 10^6 cycles, E' and tan δ were increased by 42% and decreased by 15%, respectively, indicating the presence of microcracks. Meanwhile, the baseline properties remained unchanged under both fatigue conditions. The fatigue-damping study suggested that the addition of the CNT yarns induced matrix damages such as microcracks as evident by the 15% decrease in E' at 10^6 cycles.

5.2 Recommendations

Several recommendations are suggested for the future work. The experimental results presented in this thesis could be used to develop models of damping based on the

micromechanics of hypothesized stick-slip mechanism. In order to accurately model the experimental results, the critical shear strength should be measured for different amounts of surfactant, further evaluate the resin impregnation of the CNT yarn, and also expand the mean strain study by applying wider range of strain. In addition, the dynamic properties could also be predicted with the energy method at the lamina level developed by Ni and Adams (1984). One of the ways the energy method could be used is to separate the damping of the baseline and the CNT yarns. In order to do so, unidirectional interlayer specimens with only the CNT yarn and the resin mixture need to be fabricated in the three directions—longitudinal, transverse, and shear—and then evaluated for the dynamic properties. Another interesting work that is recommended to be looked at is performing the damping test at below room temperature since rotorcrafts could also be operated under cold weather condition. Furthermore, different testing modes such as three-point bend that leads to interlaminar shear damping could also be investigated. Finally, performing acid treatment on the CNT yarns could be an interesting approach to exfoliate the yarns which could potentially allow the resin mixture to easily infiltrate the CNT yarns. However, it must be noted that the acid treatment could oxidize the CNTs, leading to covalent bonding with resin, which must be taken care of so that non-covalent bonding would form.

References

Abbe, J. T. L., Blackwell, R. H., and Jenny, D. S., 1977. "Advancing Blade Concept (ABC)™ Dynamics," 33rd *American Helicopter Society Annual Forum,* American Helicopter Society, INC, Fairfax, Virginia.

Adair, J., 2019. personal communication.

Almeras, P., 1997. "Active Control of Aeromechanical Stability Applied by Eurocopter," *23rd European Rotorcraft Forum,* Dresden, Germany.

Alva, A., and Raja, S., 2014. "Damping Characteristics of Epoxy-Reinforced Composite with Multiwall Carbon Nanotubes," *Mechanics of Advanced Materials and Structures,* 21(3):197-206.

Berg, J. C., 2010. "An Introduction to Interfaces & Colloids: the Bridge to Nanoscience," World Scientific.

Bhagat, R. B., Amateau, M. F., and Smith, E. C., 1988. "Logarithmic Decrement Measurements on Mechanically Alloyed Aluminum and SiC Particulate Reinforced Aluminum Matrix Composites," in *Proc. The International Symposium on Advances in Cast Reinforced Metal Composites: held in conjunction with 1988 World Materials Congress.* Materials Park, Ohio, USA.

Blackwell, R., and Millott, T., 2008. "Dynamics Design Characteristics of the Sikorsky X2 Technology™ Demonstrator Aircraft," *64th American Helicopter Society Annual Forum,* American Helicopter Society, INC, Fairfax, Virginia.

Chamis, C. C., and Sinclair, J. H., 1977. "Ten-Deg Off-Axis Test for Shear Properties in Fiber Composites," *Experimental Mechanics* 17(9): 339-346.

Chopra, I., 2002. "Review of state of art of smart structures and integrated systems," *AIAA Journal*, *40*(11): 2145-2187.

Daniel, I. M., Ishai, O., Daniel, I. M., and Daniel, I., 1994. "*Engineering mechanics of composite materials,"* New York: Oxford University Press.

DeValve, C., and Pitchumani, R., 2013. "Experimental Investigation of The Damping Enhancement in Fiber-Reinforced Composites with Carbon Nanotubes," *Carbon* 63(3): 71-83.

Dong, L. and Lakes, R., 2013. "Advanced Damper with High Stiffness and High Hysteresis Damping Based on Negative Structural Stiffness," *International Journal of Solids and Structures* 50(14-15):2416-2423.

Foye, R. L. and Shipley, J. L., 1981. "Evolution of the Application of Composite Materials to Helicopters," *Journal of the American Helicopter Society*, *26*(4): 5-15.

Gardea, F., Glaz, B., Riddick, J., Lagoudas, D. C., and Naraghi, M., 2016. "Energy Dissipation Due to Interfacial Slip in Nanocomposites Reinforced with Aligned Carbon Nanotubes," *ACS Applied Materials & Interfaces* 7(18): 9725-9735.

Gardea, F., Cole, D., Glaz, B., and Riddick, J., 2018. "Strain Energy Dissipation Mechanisms in Carbon Nanotube Composites Fabricated by Additive Manufacturing," *Mechanics of Additive and Advanced Manufacturing*, 9: 29-36.

Geng, Y., Liu, M. Y., Li, J., Shi, X. M., and Kim, J. K., 2008. "Effects of Surfactant Treatment on Mechanical and Electrical Properties of CNT/Epoxy Nanocomposites," *Composites Part A: Applied Science and Manufacturing*, *39*(12): 1876-1883.

Glaz, B., Riddick, J., Habtour, E., and Kang, H., 2015. "Interfacial Strain Energy Dissipation in Hybrid Nanocomposite Beams Under Axial Strain Fields," *AIAA Journal* 53(6): 1544-1554.

Gong, X., Liu, J., Baskaran, S., Voise, R. D., and Young, J. S., 2000. "Surfactant-Assisted Processing of Carbon Nanotube/Polymer Composites," *Chemistry of materials*, *12*(4): 1049-1052.

Jones, D. I., 2001. "Handbook of viscoelastic vibration damping," John Wiley & Sons.

Khan, S. U., Li, C. Y., Siddiqui, N. A., and Kim, J. K., 2011. "Vibration Damping Characteristics of Carbon Fiber-Reinforced Composites Containing Multi-Walled Carbon Nanotubes," *Composites Science and Technology* 71(12): 1486-1494.

Kim, H. W., Duraisamy, K., and Brown, R., 2009. "Effect of Rotor Stiffness and Lift Offset on the Aeroacoustics of a Coaxial Rotor in Level Flight," *65th American Helicopter Society Annual Forum*, American Helicopter Society, INC, Fairfax, Virginia.

Koratkar, N., Wei, B. Q., and Ajayan, P. M., 2002. "Carbon Nanotube Films for Damping Applications," *Advanced Materials* 14(13-14): 997-1000.

Kulak, R. F., and Hughes, T. H., 1993. "Frequency and Temperature Dependence of High Damping Elastomers," *No. ANL/RE/CP-78944*. Argonne National Lab, USA.

Liu, J., Rinzler, A.G., Dai, H., Hafner, J.H., Bradley, R.K., Boul, P.J., Lu, A., Iverson, T., Shelimov, K., Huffman, C.B. and Rodriguez-Macias, F., 1998. "Fullerene Pipes," *Science* 280(5367): 1253-1256.

Liu, B. and Haftka, R. T., 2004. "Single-Level Composite Wing Optimization Based on Flexural Lamination Parameters," *Structural and Multidisciplinary Optimization*, *26*(1-2): 111-120.

Liu, A., Huang, J. H., Wang, K. W., and Bakis, C. E., 2006. "Effects of Interfacial Friction on the Damping Characteristics of Composites Containing Randomly Oriented Carbon Nanotube Ropes," *Journal of Intelligent Material Systems and Structures* 17(3): 217-229.

Liu, Ailin, Wang, K. W., and Bakis, C. E., 2010. "Multiscale Damping Model for Polymeric Composites Containing Carbon Nanotube Ropes," *Journal of Composite Materials* 44(19): 2301-2323.

Lu, J. P., 1997. "Elastic Properties of Single and Multilayered Nanotubes," *Journal of Physics and Chemistry of Solids*," *58*(11): 1649-1652.

McGuire, D. P., 1994. "Fluidlastic Dampers and Isolators for Vibration Control in Helicopters," *50th American Helicopter Society Annual Forum*, American Helicopter Society, INC, Fairfax, Virginia.

Menard, K. P., 2008. "Dynamic Mechanical Analysis: a Practical Introduction," CRC press.

Micro-Measurements, 2011a. "Instruction Bulletin B-129-8 Strain Gage Installations with M-Bond 200 Adhesive," No.11129, Vishay Measurements Group Inc., Wendell, North Carolina, USA.

Micro-Measurements, 2011b. "Tech Note TN-509 Errors Due to Transverse Sensitivity in Strain Gages," No.11059, Vishay Measurements Group Inc., Wendell, North Carolina, USA.

Micro-Measurements, 2018. "Instruction Bulletin B-127 Strain Gage Installations with M-Bond 200 Adhesive," No.11124, Vishay Measurements Group Inc., Wendell, North Carolina, USA.

Miller-Stephenson, 2012. "EPIKOTE™ Resin 862/ EPIKURE™ Curing Agent W System," SC1183-02, Miller-Stephenson, Inc., Danbury, Connecticut, USA.

Mousa, M. S., 2018. "Comparison Between Single-Walled CNT, Multi-Walled CNT, and Carbon Nanotube-Fiber Pyrograf III," *Conference Series: Materials Science and Engineering* 305(1):12-25. IOP Publishing.

Nanocomp Technologies, 2016. "Miralon Yarn for Mechanical Applications (YM)," C-Series Yarn, Nanocomp Technologies, Inc. A Huntsman Company, Merrimack, New Hampshire, USA.

NanoTechLabs, 2017. "Buckypaper Data Sheet," Buckeye Composites NanoTechLabs, Inc., Yadkindville, North Carolina, USA.

Ni, R. G., and Adams, R. D., 1984. "The Damping and Dynamic Moduli of Symmetric Laminated Composite Beams—Theoretical and Experimental Results," *Journal of Composite Materials*, *18*(2): 104-121.

Ogasawara, T., Tsuda, T., and Takeda, N., 2011. "Stress–Strain Behavior of Multi-Walled Carbon Nanotube/PEEK Composites," *Composites Science and Technology* 71(2): 73-78.

Paglino, V. M., 1971. "Forward Flight Performance of a Coaxial Rigid Rotor," *27th American Helicopter Society Forum*, American Helicopter Society, INC, Fairfax, Virginia.

Parfitt, G. D. and Rochester, C. H., 1983. "Adsorption from Solution at the Solid/Liquid Interface," London: Academic press.

Pindera, M. J., and Herakovich, C. T., 1986. "Shear Characterization of Unidirectional Composites with the Off-Axis Tension Test," *Experimental Mechanics* 26(1): 103-112.

Poutrel, Q. A., Wang, Z., Wang, D., Soutis, C., and Gresil, M., 2017. "Effect of Pre And Post-Dispersion on Electro-Thermo-Mechanical Properties of a Graphene Enhanced Epoxy," *Applied Composite Materials, 24*(2): 313-336.

Prakash, K., Smith, E. C., and Bakis, C. E., 2018. "Modeling of Polymer/Carbon Nanotube Nanocomposite to Estimate Structural Damping in a Rotorcraft Blade," *33rd American Society for Composites,"* Seattle, Washington, USA.

Prakash, K., Smith, E. C., and Bakis, C. E., 2019. "Modeling of Laminated Reinforced Composite with Carbon Nanotube Interlayers to Estimate Structural Damping in a Rotorcraft Blade," *AIAA Scitech 2019 Forum*, American Helicopter Society, INC, Fairfax, Virginia.

Rajoria, H., and Jalili, N., 2005. "Passive Vibration Damping Enhancement Using Carbon Nanotube-Epoxy Reinforced Composites," *Composites Science and Technology* 65(14): 2079-2093.

Rastogi, R., Kaushal, R., Tripathi, S. K., Sharma, A. L., Kaur, I., and Bharadwaj, L. M., 2008. "Comparative Study of Carbon Nanotube Dispersion Using Surfactants," *Journal of colloid and interface science, 328*(2): 421-428.

Rudin, A. and Choi, P., 2012. "The Elements of Polymer Science and Engineering," Academic press.

Sharma, Ambuj, 2010. "Controlling Dispersion and Electric-Field-Assisted Alignment of Carbon Nanotubes and Nanofibers for Multi-functional Epoxy Composites," Ph.D. Dissertation, The Pennsylvania State University, University Park, Pennsylvania.

Sugime, H., Esconjauregui, S., Yang, J., D'Arsié, L., Oliver, R. A., Bhardwaj, S., Cepek, C., and Robertson, J., 2013. "Low Temperature Growth of Ultra-High Mass Density Carbon Nanotube Forests on Conductive Supports," *Applied Physics Letters* 103(7): 073116.

Suhr, J., Koratkar, N., Keblinski, P., and Ajayan, P., 2005. "Viscoelasticity in Carbon Nanotube Composites," *Nature materials* 4(2): 134.

Suhr, J., Koratkar, N. A., Ye, D. and Lu, T. M., 2006. "Damping Properties of Epoxy Films with Nanoscale Fillers," *Journal of intelligent material systems and structures*, *17*(3):255-260.

Tanimoto, T., Horiuchi, K., and Uchino, K., 1997. "Passive Damping Performance of an Adaptive Carbon-Fiber Reinforced Plastics/Lead Zirconate Titanate Beam," *Japanese journal of applied physics*, *36*(9S):6110.

Tanimoto, T., 2007. "A New Vibration Damping CFRP Material with Interlayers of Dispersed Piezoelectric Ceramic Particles," *Composites science and technology*, *67*(2): 213-221.

Van Humbeeck, J., 2003. "Damping Capacity of Thermoelastic Martensite in Shape Memory Alloys," *Journal of Alloys and Compounds*, *355*(1-2): 58-64.

Vashisth, A., Bakis, C. E., Ruggeri, C. R., Henry, T. C. and Roberts, G. D., 2018. "Ballistic Impact Response of Carbon/Epoxy Tubes with Variable Nanosilica Content," *Journal of Composite Materials*, *52*(12):1589-1604.

Wang, Z., Liang, Z., Wang, B., Zhang, C., and Kramer, L., 2004. "Processing and Property Investigation of Single-Walled Carbon Nanotube (SWNT) Buckypaper/Epoxy Resin Matrix Nanocomposites," *Composites Part A: Applied Science and Manufacturing* 35(10): 1225-1232.

Wang, M. S., Golberg, D., and Bando, Y., 2010. "Tensile Tests on Individual Single-Walled Carbon Nanotubes: Linking Nanotube Strength with Its Defects," *Advanced Materials*, *22*(36): 4071-4075.

Wang, S., Downes, R., Young, C., Haldane, D., Hao, A., Liang, R., Wang, B., Zhang, C., and Maskell, R., 2015. "Carbon Fiber/Carbon Nanotube Buckypaper Interply Hybrid Composites: Manufacturing Process and Tensile Properties," *Advanced Engineering Materials*, *17*(10):1442-1453.

Yu, M. F., Lourie, O., Dyer, M. J., Moloni, K., Kelly, T. F., and Ruoff, R. S., 2000. "Strength and Breaking Mechanism of Multiwalled Carbon Nanotubes under Tensile Load," *Science*, *287*(5453): 637-640.

Zhou, X., Shin, E., Wang, K. W., and Bakis, C. E., 2004. "Interfacial Damping Characteristics of Carbon Nanotube-Based Composites," *Composites Science and Technology* 64(15): 2425-2437.

Appendix A

Auxiliary Data

Table A-1: CNT:TX mass ratio calculation (g).

1	2	3	4	5	6	7	8
100 mL beaker	580 pieces of 2.54-cm long CNT yarn	862/W	TX	862/W+TX in beaker after dipping and removing yarns	862/W+TX in the c/ep	TX in the c/ep	CNT:TX ratio
9.897	0.239	8.711	8.911	25.740	2.018	1.009	1:4.2
9.754	0.236	6.520	6.506	21.059	1.957	0.489	1:2.1

The mass of the 862/W and TX in the c/ep is calculated by first adding columns 1 through 4 and then subtracting column 5, leading to the mass of 862/W and TX in the c/ep laminate (column 6). Depending on the mass ratio of 862/W:TX, either 50% (1:1) or 25% (1:0.25) is multiplied to column 6 to get the TX mass in the c/ep (Column 7). Column 7 is then divided by column 2 in order to obtain the mass ratio of CNT to TX, which is presented in column 8. It is assumed throughout the calculation that TX does not spread into other region but instead stays close to the CNT yarns.

Table A-2: Comparison of fiber volume contents measured by image analysis of images collected at 500× and 5000×.

500×		**5000×**	
Avg (%)	**Sdev. (%)**	**Avg (%)**	**Sdev. (%)**
76.10	2.02	76.04	1.88

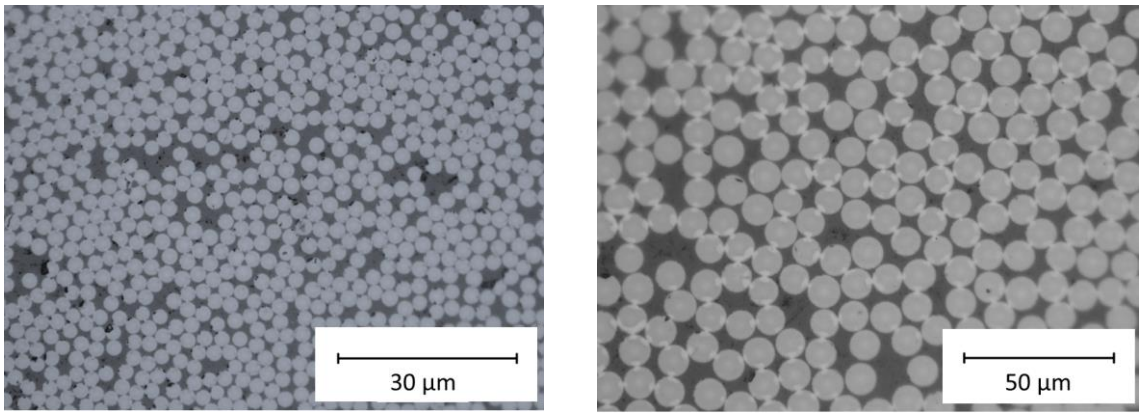

a) b)

Figure A-1: Cross-sectional area of $[90]_6$ baseline laminate with 77% V_f at a) 500× and b) 5000×.

Table A-3: Test variation of the phase lag collected from three strain measurement techniques.

Material	Technique	Test Repetition 1	2	3	4	Avg.	Sdev.	CV (%)
862W	Exten. CA[1]	0.0109	0.0088	0.0097	0.0093	0.0097	0.0009	9.3
	Exten. Si[2]	0.0072	0.0103	0.0088	0.008	0.0086	0.0013	15.4
	Strain gage[3]	0.0072	0.0066	0.0071	0.0065	0.0069	0.0004	5.1
PU	Exten. CA	0.0323	0.0343	0.0322	0.0311	0.0325	0.0013	4.1
	Exten. Si	0.0357	0.034	0.0344	0.0312	0.0338	0.0019	5.6
	Strain gage	0.0261	0.0246	0.0257	0.0241	0.0251	0.0009	3.7
Al	Exten. CA	0	-0.0046	-0.0049	-0.0055	-0.0037	0.0025	-67.4
	Exten. Si	-0.0049	-0.0008	-0.0065	-0.0017	-0.0035	0.0027	-77.0
	Strain gage	-0.0080	-0.0081	-0.0086	-0.0083	-0.0083	0.0003	-3.2

[1]One extensometer with v-notched tabs bonded to specimen using cyanoacrylate adhesive
[2]One extensometer with v-notched tabs bonded to specimen using silicone adhesive
[3]One strain gage

Table A-4: Void (V_v), matrix (V_m), and fiber (V_f) volume fractions measured in 30 images of a $[90]_6$ baseline laminate, obtained using image analysis and 500× magnification.

Image #	V_v **(%)**	V_m **(%)**	V_f **(%)**
image1	0.39	41.2	58.5
image2	1.3	43.4	55.3
image3	0.29	39.8	59.9
image4	0.21	36.1	63.7
image5	0.23	37.5	62.3
image6	0.36	35.6	64.1
image7	0.61	34.7	64.7
image8	1.13	39.4	59.5
image9	0.4	36.3	63.4
image10	0.21	33.8	66.0
image11	0.47	38.9	60.6
image12	0.44	37.7	61.8
image13	0.7	37.4	61.9
image14	0.4	43.0	56.6
image15	0.25	38.2	61.6
image16	0.37	37.6	62.0
image17	0.61	39.2	60.2
image18	1.67	39.2	59.1
image19	0.65	39.5	59.8
image20	0.3	41.4	58.3
image21	0.45	41.3	58.3
image22	0.3	38.0	61.7
image23	0.28	36.5	63.2
image24	0.24	38.8	61.0
image25	0.32	39.2	60.5
image26	0.82	35.4	63.8
image27	0.44	34.3	65.3
image28	0.32	35.2	64.5
image29	0.26	42.5	57.3
image30	0.95	40.2	58.9
Average	0.51	38.4	61.1
Sdev.	0.35	2.6	2.7

Table A-5: Void volume fractions measured in 29 images of a $[90]_6$ YN10%-TX4 laminate, obtained using image analysis and 500× magnification.

Image #	V_v **(%)**
image7	0.06
image8	0.05
image9	0.15
image10	0.16
image11	0.33
image12	0.56
image13	0.62
image14	0.09
image15	0.03
image16	0.18
image17	2
image18	1.95
image19	0.06
image20	0.12
image21	0.17
image22	0.04
image23	0.12
image24	0.01
image25	0.1
image26	0.27
image27	0.02
image28	0.06
image29	2.43
image30	1.03
image31	0.39
image32	1.67
image33	0.26
image34	0.04
image35	0.12
Average (%)	0.45
Sdev.	0.68

Table A-6: Dynamic properties of $[0/\pm45]_s$ baseline and YN10%-TX4 at different strain excursions.

Material	με	tan δ	E' (GPa)	E'' (MPa)
Baseline	180-390	0.0034	54	184
	190-2030	0.0037	55	203
	180-3180	0.0053	56	293
	180-4230	0.0071	56	396
	200-5260	0.0086	56	482
YN10%-TX4	140-250	0.0111	59	650
	140-300	0.0125	58	729
	150-350	0.0136	58	788
	150-400	0.0147	58	849
	150-450	0.0155	58	893
	150-510	0.0162	58	930
	150-560	0.0167	57	957
	160-770	0.0191	57	1086
	160-1030	0.0201	57	1138
	170-1540	0.0218	57	1233
	160-2050	0.0234	57	1330
	170-2560	0.0249	57	1425
	170-3050	0.0263	58	1518
	190-3540	0.0277	58	1614
	200-4040	0.0292	59	1715
	230-4520	0.0308	59	1826
	250-5010	0.0323	60	1932

Table A-7: Dynamic properties of $[0/\pm45]_s$ baseline and YN10%-TX4 at different mean strain and constant strain amplitude of 250 με.

Material	Mean strain (με)	tan δ	E' (GPa)	E'' (MPa)
Baseline	266	0.0033	54	178
	1070	0.0037	55	203
	1880	0.0044	56	245
YN10%-TX4	250	0.0191	56	1067
	520	0.0201	56	1132
	790	0.0203	57	1157
	1070	0.0204	58	1179
	1340	0.0201	59	1183
	1610	0.0199	60	1195
	1880	0.0198	61	1216

Table A-8: The effect of fatigue cycles on the dynamic properties of $[0/\pm45]_s$ YN10%-TX4 laminate at the fatigue frequency of 10 Hz and the fatigue strain of 300-3000 με.

Repetition	**Damping Freq. (Hz)**	**Maximum number of cycles**	**Damping strain (με)**	**tan δ**	***E'* (GPa)**	***E"* (MPa)**
1	1	10^2	180-1550	0.0243	56	1365
		10^3	180-1540	0.0243	56	1365
		10^4	190-1560	0.0239	56	1335
		10^5	180-1570	0.0258	55	1422
		4×10^5	190-1590	0.0265	54	1443
		7×10^5	190-1600	0.0267	54	1447
		10^6	200-1610	0.0268	54	1446
2	1	10^2	190-1560	0.0255	56	1432
		10^3	180-1550	0.0254	56	1426
		10^4	190-1560	0.0250	56	1400
		10^5	190-1570	0.0256	55	1411
		4×10^5	190-1600	0.0270	54	1470
		7×10^5	200-1610	0.0272	54	1473
		10^6	200-1610	0.0285	54	1538

Table A-9: The effect of fatigue cycles on the dynamic properties of $[0/\pm45]_s$ YN10%-TX4 laminate at the fatigue frequency of 10 Hz and the fatigue strain of 300-4000 με.

Repetition	Damping Freq. (Hz)	Maximum number of cycles	Damping strain (με)	tan δ	E' (GPa)	E'' (MPa)	NOTE
1	1	0	180-1550	0.0218	58	1274	-
		10^2	190-1580	0.0232	58	1342	-
		10^3	200-1600	0.0223	57	1279	-
		10^4	190-1620	0.0239	56	1349	-
		10^5	210-1680	0.0287	54	1558	New strain gage
		10^6	170-1500	0.0305	50	1510	New strain gage
2	1	0	190-1560	0.0215	59	1256	-
		10^2	180-1570	0.0221	58	1279	-
		10^3	190-1580	0.0228	58	1310	-
		10^4	190-1610	0.0243	57	1374	-
		10^5	190-1670	0.0282	54	1531	New strain gage
		10^6	170-1510	0.0308	50	1525	New strain gage

Table A-10: The effect of fatigue cycles on the dynamic properties of $[0/\pm45]_s$ baseline laminate at the fatigue frequency of 10 Hz and the fatigue strain of 300-3000 με.

Repetition	Damping Freq. (Hz)	Maximum number of cycles	Damping strain (με)	tan δ	E' (GPa)	E'' (MPa)
1	1	0	200-1560	0.0041	57	233
		10^2	190-1530	0.0045	57	255
		10^3	190-1530	0.0046	57	261
		10^4	190-1540	0.0045	57	255
		10^5	190-1540	0.0048	57	272
		4×10^5	190-1540	0.0048	57	272
		7×10^5	190-1540	0.0047	57	267
		10^6	190-1540	0.0043	57	244
2	1	0	180-1530	0.0041	57	233
		10^2	170-1520	0.0044	57	250
		10^3	190-1530	0.0044	57	250
		10^4	190-1530	0.0046	57	261
		10^5	190-1530	0.0048	57	272
		4×10^5	190-1530	0.0047	57	267
		7×10^5	190-1530	0.0047	57	267
		10^6	190-1530	0.0045	57	255

Table A-11: The effect of fatigue cycles on the dynamic properties of $[0/\pm45]_s$ baseline laminate at the fatigue frequency of 10 Hz and the fatigue strain of 300-4000 με.

Repetition	**Damping Freq. (Hz)**	**Maximum number of cycles**	**Damping strain (με)**	**tan δ**	***E'* (GPa)**	***E"* (MPa)**	**NOTE**
1	1	0	200-1560	0.0029	49	141	-
		10^2	170-1520	0.0034	49	165	-
		10^3	170-1530	0.0034	49	165	-
		10^4	170-1530	0.0038	49	185	-
		10^5	200-1540	0.0033	50	164	-
		10^6	170-1520	0.0029	50	143	New strain gage
2	1	0	170-1520	0.0030	49	146	-
		10^2	160-1510	0.0033	49	160	-
		10^3	170-1520	0.0034	49	165	-
		10^4	160-1520	0.0036	49	175	-
		10^5	180-1510	0.0038	50	189	-
		10^6	170-1510	0.0030	50	148	New strain gage

Table A-12: The effect of fatigue cycles on the dynamic properties of $[0/\pm45]_s$ baseline laminate at the fatigue frequency of 10 Hz and the fatigue strain of 300-4000 με.

Repetition	**Damping Freq. (Hz)**	**Maximum number of cycles**	**Damping strain (με)**	**tan δ**	***E'* (GPa)**	***E"* (MPa)**
1	1	10^2	210-1570	0.0218	53	1146
		10^3	180-1470	0.0216	52	1129
		10^4	210-1500	0.0230	52	1198
		10^5	190-1490	0.0234	51	1205
2	1	10^2	180-1540	0.0214	53	1126
		The damping tested performed only once at 10^3				
		10^4	170-1460	0.0223	52	1163
		10^5	180-1480	0.0232	51	1195

Table A-13: The temperature effect on the dynamic properties of $[0/\pm45]_s$ laminate.

Material	Temperature (°C)	Strain range (με)	tan δ	E' (GPa)	E'' (MPa)
Baseline	22.2	190-1520	0.00347	56	193
	45	180-1530	0.00377	55	207
	65	200-1580	0.00377	54	205
YN10%-TX4	22.2	190-1540	0.02337	58	1353
	45	150-1490	0.02508	56	1411
	65	160-1500	0.02628	54	1432

Table A-14: Tensile strength (F_{xt}) of $[0/\pm45]_s$ baseline and YN10%-TX4 laminate.

Specimen	Specimen #	F_{xt} (MPa)	Average (MPa)	CV (%)
Baseline	1	700	677±38	5.6
	2	698		
	3	633		
YN10%-TX4	1	680	660±57	8.6
	2	705		
	3	596		

Table A-15: Material specification of the soft type II 207 PZT.

Property	Symbol	Type II[1]
		207
Density (g/cm^3)	ρ	7.95
Curie point (˚C)	T_c	370
Permittivity	K^T_{33}	2100
Dielectric loss	tan δ	0.018
Anti-electric power (kV/cm)	E_c	16
Piezoelectric constant in the polarization direction (pm/V)	d_{33}	450
Piezoelectric constant in the longitudinal direction (pm/V)	d_{31}	-202
Piezoelectric constant in the Shear direction (pm/V)	d_{15}	550
Coupling factor in the polarization direction	k_{33}	0.72
Coupling factor in the thickness direction	k_t	0.5
Coupling factor in the radial direction	k_p	0.67
Coupling factor in the shear direction	k_{15}	0.68
Frequency constant radial direction	N_p	unknown
Frequency constant thickness direction	N_t	Unknown

[1] the information was obtained from the website of the TRS Technologies Inc.

Table A-16: Volume fraction calculation for GBP, VDP, SMA-H, PU veil, and PZT.

Material Type	Equation
GBP	$V_{GBP} = \frac{t_{GBP} \cdot n_{int}}{t_{lam}} \rho \cdot 100\% = 6.1\%$
VDP	$V_{VDP} = \frac{t_{VDP} \cdot n_{int}}{t_{lam}} \cdot 100\% = 12.5\%$
SMA-H	$V_{SMA} = \frac{n_{int} \cdot n_w \cdot A_w}{A_{lam}} \cdot 100\% = 2.4\%$
PU veil	$V_{PU} = \frac{A_{PU}}{A_{lam}} \cdot 100\% = 1\%$
PZT	$V_{PZT} = \frac{A_{PZT}}{A_{plate}} \cdot 100\% = 0.5\%$

t_{GBP} = thickness of GBP = 0.0025 cm
t_{VDP} = thickness of VDP = 0.005 cm
t_{lam} = thickness of 6-layer c/ep laminate = 2 cm
ρ = carbon content in GBP = 97%
n_{int} = number of interlayers = 5
n_w = number of SMA in one interlayer = 5
d_w= diameter of SMA = 0.025 cm
A_w = area of SMA = $\frac{\pi d_w^2}{4}$ = 0.000487 cm^2
A_{lam}= cross-sectional area of a 2.54-cm wide and 0.2-cm thick laminate = 0.508 cm^2
A_{plate}= cross-sectional area of 10.5-cm wide and 0.2-cm thick plate = 2.095 cm^2
m_{PZT}= weighed PU PZT = 0.8233 g
ρ_{PZT}= density of PZT = 7.95 g/cm^3
l_{PZT}= length of PZT plate = 10.5 cm
A_{PZT} = area of PZT = $\frac{\frac{m_{PZT}}{\rho_{PZT}}}{l_{PZT}}$ = 0.00988 cm^2
m_{PU}= weighed PU mass = 0.015 g
ρ_{PU}= density of PU = 1.12 g/cm^3
l_{PU}= length of PU = 2.54 cm
A_{PU}= area of PU = $\frac{\frac{m_{PU}}{\rho_{PU}}}{l_{PU}}$ = 0.00527 cm^2

Appendix B

Damping Matlab Code

```
%%
clear all
clc

% read in a data file and assgining variables for each column
filename='damping(1x10^3)-1.xlsx';    % raw data file
A=xlsread(filename);

X=[A(:,1),A(:,8),A(:,13)];  % For damping specimen: columns 8,13 / For Aluminum cal
specimen: columns 2,3

Time = X(2:end,1)';
Stress = X(2:end,2)';
Strain = X(2:end,3)';

% Finding the domain(x-axis) frequency in hertz
LL=length(Strain)          % length of the signal vector (number of sample)
Fs = 150;                  % sampling frequency
DF = Fs/length(Strain);    % frequency increment
freqvec = 0:DF:Fs/2;       % frequency in hertz

% Using Fast Fourier Transform to convert from time domain to frequency
% domain
X= fft(Strain);   % Fast Fourier Transform gives the raw data file in complex number
X=X(2:end);      % The first element, frequency bin at zero is the sum of all the elements, which
is an unnecessary value. Ref. DFT equation
Y= fft(Stress);
Y=Y(2:end);
[k, indx] = max(abs(X));    % finding the index of the dominant frequency
[l, indy] = max(abs(Y));     % indx and indy must be the same since both signals have the same
principle frequency.
angleload = angle(Y(indx))
angledis = angle(X(indx))
PhDiff_rad = angleload-angledis      % Phase difference of the two phase angles wrt origin
PhDiff_angle = PhDiff_rad*180/pi    % Phase difference in angle

dynModConst = l/k*10^6            % Dynamic modulus

% Graphing spectrum of signals in frequency domain
xdft = X(1:length(Strain)/2+1);     % cutting the domain by half because half of the domain is
mirrored.
xdft = abs(xdft);                    % magnitude of each frequency in the signal
```

```
ydft = Y(1:length(Stress)/2+1);
ydft = abs(ydft);

figure
plot(freqvec(2:end), xdft(2:end))   % again, the first element is the frequency Bin at zero
xlabel('Frequency (Hz)')            % X-axis
ylabel('Disp. Amplitdude')          % Y-axis

figure
plot(freqvec(2:end), ydft(2:end))
xlabel('Frequency (Hz)')
ylabel('Load Amplitdude')

% Supper imposing the displacement and load signal
figure
hold on
xlim([0,400])
plot(Strain/max(Strain))
plot(Stress/max(Stress))
legend('disp','load')
ylabel('normalized disp, load')
xlabel('# of points')
hold off
box on

MagS = abs(xdft(indx));
Noise = [xdft(1:indx), xdft(indx:end)];
MagN = mean(abs(Noise))

SNR = MagS/MagN % Signal to  noise
```

Appendix C

Non-Technical Abstract

Carbon/epoxy (c/ep) composite is a well-known material for lightweight structures due to its high strength to weight ratio. As a result, c/ep composites are desired in rotorcraft blades that need to be light so that the amount of fuel can be conserved. However, c/ep composites do not minimize vibrations enough. Successfully minimizing the vibration could lead to an advanced design of rotorcrafts that have stabile flight control. Recently, studies have shown that adding carbon nanotubes (CNTs) to polymers could increase damping. These embedded CNTs that are bonded weakly to the resin could continue to slip and stick back to the resin when they are stretched and unstretched. During this process, the CNTs can dissipate energy through the friction. The main study is to enhance the damping of c/ep composite with the CNTs without reducing the structural integrity and then investigate the damping under different conditions.

Three different forms of CNTs were evaluated for damping. Long CNTs in a yarn form or sheet form and short CNTs in a sheet form were investigated. In order to adjust the bond strength between the CNTs and the resin, two different surfactants were applied. As rotorcrafts are often operated under various conditions, c/ep composites with CNTs were tested at different temperature, strain, and fatigue life. Elevated temperature moderately increased damping, while the High strain that was applied to the CNTs after a certain point at which the CNTs slipped increased damping. Damping of CNTs was consistent for the first 100,000 fatigue cycles but started to increase afterwards due to possible damages and failure of the resin.